Online Parallel Estimation of Mechanical Parameters for PMSM Drives via a Network of Interconnected Extended Sliding-Mode Observers

Chengbo Yang, *Student Member, IEEE*, Bao Song, Yuanlong Xie, *Member, IEEE*, and Xiaoqi Tang

***Abstract*—The accurate estimation of mechanical parameters is essential for the control optimization and condition monitoring of permanent-magnet synchronous motor (PMSM) drives. In this article, an online parallel estimation scheme is proposed based on a network of three interconnected extended sliding-mode observers. With a two-step mechanism derived from the developed network, this scheme can simultaneously achieve the accurate real-time observation of three mechanical parameters, including the viscous friction coefficient, the moment of inertia, and the load torque. The first step utilizes the presented network to precisely acquire the Coulomb friction coefficient by offering only one speed. With aiding from this estimated coefficient, the second step attains the high-precision online identification of the three concerned parameters by compensating the Coulomb friction torque to counteract its adverse effect. These two steps are implemented utilizing the identical network, thus, furthest avoiding increasing the estimation complexity. Besides, any additional knowledge other than the rotor speed and electromagnetic torque is no longer required for guaranteeing the asymptotic convergence of the estimation errors. Sufficient evaluations from simulations and experiments confirm the validity of the proposed scheme.**

***Index Terms*—Extended sliding-mode observer (ESMO), mechanical parameters, parallel estimation, permanent-magnet synchronous motor (PMSM).**

I. INTRODUCTION

CURRENTLY, due to the high reliability and superior torque-to-inertia ratio, permanent-magnet synchronous motors (PMSMs) are attracting widespread interest in various applications, ranging from industrial robots, electric vehicles, and medical devices [1]–[3]. In a PMSM-based drive system, the accurate knowledge of the mechanical parameters is indispensable to achieve high-performance control and monitor system conditions. Conventionally, the PMSM system's mechanical parameters include the Coulomb and viscous friction coefficients, the moment of inertia, and the load torque. Nevertheless, these parameters are immeasurable in practice, implying that they cannot be acquired directly [4]. In general, identification algorithms are used for estimating these parameters. Since the viscous friction torque is dominant in the total friction torque during the drive system operation [5], more attention is being paid to identifying three pivotal mechanical parameters, including the moment of inertia of the entire system, the load torque, and the viscous friction coefficient [6], [7].

Numerous parameter estimation approaches pertaining to this research area has been put forward, which can be mainly classified into six categories: sliding-mode observer (SMO)-based stepwise estimation [6]–[9], extended Kalman filter (EKF) [10], [11], model reference adaptive system (MRAS) [12], [13], recursive least squares (RLS) [4], [14], [15], algebraic parameter identification (API) [16], [17], and online parallel estimation [18]–[24]. These methods are potential candidates for estimating the three mechanical parameters. It is noteworthy that with the exception of the MRAS, other methods have been successfully employed to identify the three concerned parameters (e.g., [4], [6], [10], [16], and [23]). Indeed, when the MRAS is applied for multiparameter estimation, its adaptive mechanism design is rather challenging. Moreover, the MRAS is subject to poor robustness. These imperfections may restrict its further applications. Although the other five methods have been applied to the concerned area, challenges remain for practical utilizations of these candidates.

The SMO-based stepwise estimation method is commonly used for acquiring the three mechanical parameters and has been reported widely. In [6], a three-step manner was utilized to extract the three parameters from the lump disturbance observed by a high-order SMO. Similarly, in [7]–[9], relying on the system disturbance identified from the extended SMO (ESMO), the three concerned parameters were determined in three steps. Although the abovementioned methods are capable of gaining positive results, there exist some challenges for practical usages. *First,* these methods are not applicable to an application where both the load torque and the inertia are time-varying. Typical examples involve industrial robots [25], mechanical elastic energy storage devices [26], and electric winding machines [27]. *Second,* in these methods, the viscous friction coefficient's

---

Manuscript received November 1, 2020; revised February 11, 2021; accepted March 14, 2021. Date of publication March 18, 2021; date of current version June 30, 2021. This work was supported in part by the National Key R&D Project under Grant SQ2019YFB1707300, in part by the Major Science and Technology Project of Guangdong Province under Grant 2020B090927001, in part by the China Postdoctoral Science Foundation under Grant 2019M650179, and in part by the National Natural Science Foundation of China under Grant 51975430. Recommended for publication by Associate Editor U. Deshpande. *(Corresponding author: Bao Song.)*

The authors are with the State Key Laboratory of Digital Manufacturing Equipment and Technology and National NC System Engineering Research Center, School of Mechanical Science and Engineering, Huazhong University of Science and Technology, Wuhan 430074, China (e-mail: cb_yang@hust.edu.cn; songbao@hust.edu.cn; yuanlongxie@hust.edu.cn; xqtang@hust.edu.cn).

Color versions of one or more figures in this article are available at https://doi.org/10.1109/TPEL.2021.3067328.

Digital Object Identifier 10.1109/TPEL.2021.3067328

estimation requires the drive system to be operated at two different constant speeds, which restricts its online identification during normal operation. It is noteworthy that this online-estimation demand is vital for monitoring the mechanical system [28], [29]. Moreover, in many scenarios, such as robots, constant speed operation may be limited for safety reasons. Altogether, this type of method may be hard to satisfy the growing needs of practical applications.

Fortunately, the remaining candidates, including the EKF, RLS, API, and online parallel estimation, are able to cope with the previously mentioned deficiencies. These methods can accomplish the simultaneous online estimation of multiple mechanical parameters. However, it should be pointed out that the EKF suffers from complex matrix operations, and its covariance matrix design poses some challenges [11]. Applying the API and RLS to the three-parameter estimation, the complicated calculations remain present, including the matrix and/or multiple integral operations [4], [16]. Moreover, both approaches are constrained by poor robustness. The abovementioned issues cause difficulties for the real-time implementations of the EKF, RLS, and API. In contrast, the online parallel estimation method can reduce the identification dimension, thereby avoiding complex matrix operations and saving computational resources. This makes the method draw significant attention from the viewpoint of applications. In [18], a robust scheme integrating a frequency-domain algorithm and a Gopinath observer was utilized to estimate the inertia and the load torque parallelly. Note that these two parts are connected by updating parameters to each other. In [19], the parallel estimation for the load torque and the inertia was performed considering different operating states. In [20]–[22], the parallel-estimation idea can also be found. It should be noted that the abovementioned methods only achieve the online observation of the load torque and the inertia but do not remove the restriction on estimating the viscous friction coefficient. Fortunately, several schemes have been reported to enable the online parallel estimation of the three parameters. In [23], an integrated strategy was developed to determine the three parameters simultaneously, which employs a disturbance observer and an integral adaptive method to estimate the load torque and the viscous friction coefficient together with the inertia, respectively. In [24], an adaptive-observer-based online-parallel-estimation idea was offered to identify the three concerned parameters. Notably, the abovementioned two schemes do not discuss the robustness of the respective method.

In fact, the online parallel estimation scheme is a mechanical-motion-equation-based method. Thus, neglecting the Coulomb friction torque will inevitably sacrifice the estimation accuracy of the three concerned parameters, especially in some applications with a large Coulomb friction coefficient. Unfortunately, all current online-parallel-estimation schemes ignore the potential adverse effects of the Coulomb friction torque. Moreover, to date, no study relating to this research area has considered the asymptotic convergence of the estimation errors of the three parameters, except the one by Zhao *et al.* [24]. However, the method offered in [24] may be problematic to guarantee the asymptotic convergence, since it requires accurate acceleration information. Actually, it is difficult to acquire precise acceleration knowledge [30], [31]. Overall, the online parallel estimation of the three concerned parameters still faces the following challenges to reach its full potential.

1) Removing the adverse effect of Coulomb friction torque is indispensable for improving the estimation accuracy. Although some methods have been presented to determine the Coulomb friction coefficient [4], [32], they have no relevance to the online parallel estimation of the three considered parameters. Employing these methods to eliminate the mentioned effect will notably increase the estimation complexity due to lacking relevance.
2) Only the rotor speed and electromagnetic torque are necessary for identifying the mechanical parameters [33]. It may be unreasonable for the asymptotic convergence to rely on the additional plant knowledge except for the rotor speed and electromagnetic torque (e.g., the acceleration). This additional demand may reduce the reliability of the asymptotic convergence and even cause nonconvergence. Moreover, such knowledge is usually unavailable or hard-to-obtain.
3) The real PMSM drive system is easily interfered with by noise [18], which results in the contamination of the rotor speed and electromagnetic torque, thereby deteriorating the parameter-estimation accuracy. Thus, the robustness against noise of the online parallel estimation scheme is a crucial problem that should be considered.

To deal with these issues, a state-interconnection-based online parallel estimation method is proposed in this article. The dominating contributions of this article are summarized below.

1) Inspired by the extended-state idea [9], [19], the three mechanical parameters are extended as new system states in this article. Then, based on the ESMO methodology [9], three novel ESMOs are developed to estimate these states. Different from the conventional ESMOs (e.g., [8], [9], and [19]), each proposed ESMO devises an equivalent derivative with time-varying feedback gain utilizing the knowledge of the mechanical parameters. Through such design, the asymptotic convergence of the parameter estimation errors is guaranteed. This is the first time that the ESMO technique is exploited to accomplish the simultaneous estimation of the three parameters, which enriches the candidate methods concerning acquiring the three parameters. The resolved vital issue during the design lies in the convergence assurance of parameter estimates.
2) Based on the proposed ESMOs, a network of three interconnected ESMOs is developed, in which the three ESMOs run in parallel and exchange information about their respective extended states in real time. Also, the global stability of the network is guaranteed. In terms of the presented network, an online parallel estimation scheme is proposed. It utilizes a two-step mechanism to achieve the accurate real-time observation of the three concerned parameters by counteracting the adverse effect of the Coulomb friction torque. It should be underlined that the two steps can share one network. This relevance

furthest avoids increasing the estimation complexity and enhances parameter identification efficiency.

3) In comparison with the existing parallel-estimation schemes, the estimation errors obtained from our scheme can be governed to be asymptotically convergent without resorting to any additional plant knowledge. This benefits from the ingenious equivalent derivatives design and the state interconnection. The presented scheme is robust against noise, which confers our scheme a significant advantage in a practice application. Besides, the extra chattering suppression is unnecessary because each presented ESMO has the low-pass filter (LPF) property, which allows smoothing the estimation result while maintaining a high switching gain. Abundant results yielded from simulations and experiments are presented to manifest the superior performance of our scheme.

The remainder of this article is organized as follows. Section II outlines the mathematical model of the PMSM. In Section III, the network of three interconnected ESMOs is proposed, and the online parallel estimation scheme is designed. Then, simulation and real-time experimental investigations are presented in Section IV. Meanwhile, performance comparisons with previous work are given to reveal the attractive advantages for our scheme. Lastly, Section V concludes this article.

II. MATHEMATICAL MODEL OF PMSM

In the rotor *d-q* coordinates, the dynamics of a PMSM can be outlined as follows:

$$u_q = R_m i_q + (i_d L_d + \psi_f)\omega_e + L_d \dot{i}_d \tag{1}$$

$$u_d = R_m i_d - i_q L_q \omega_e + L_q \dot{i}_q \tag{2}$$

$$T_e = 1.5 P_n(\psi_f + (L_d - L_q) i_d) i_q \tag{3}$$

$$J\dot{\omega}_m = T_e - T_L - B\omega_m - C\text{sign}(\omega_m) \tag{4}$$

where $u_d, u_q, i_d, i_q, L_d, L_q, P_n, R_m, \psi_f, \omega_e, \omega_m, T_e, C, T_L, J$ and *B* are the *dq*-axis voltages, *dq*-axis currents, *dq*-axis inductances, pole pair, stator resistance, rotor permanent-magnet flux linkage, electrical angular speed, rotor speed, electromagnetic torque, Coulomb friction coefficient, load torque, moment of inertia, and viscous friction coefficient, respectively.

The field-oriented vector control scheme is usually utilized to control a PMSM system. Under this scheme, the decoupling of the magnetic field and the torque can be achieved so that the PMSM possesses the control performance similar to that of a dc motor. Fig. 1 depicts the typical control structure of the vector-controlled PMSM drive system, which mainly consists of the speed-loop PI controller, the current-loop PI controllers, the PWM voltage source inverter, the position encoder, and the PMSM. For a PMSM drive system, the three key mechanical parameters, including T_L, *J*, and *B*, are immeasurable but crucial for the speed-loop control performance optimization and condition monitoring. Therefore, it is necessary to identify these parameters. Given this context, this article focuses on the simultaneous online observation of the parameters T_L, *J*, and *B*, and an online-parallel-estimation method is developed to serve this purpose.

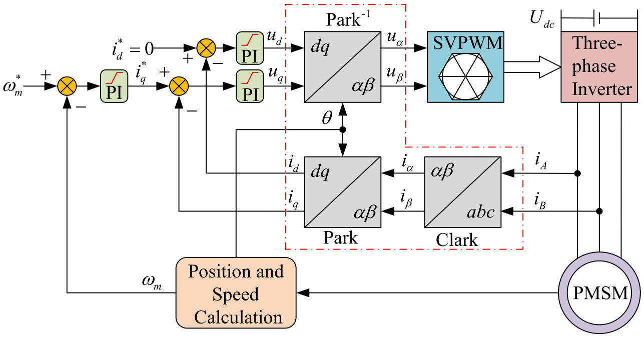

Fig. 1. Schematic diagram of the vector-controlled PMSM drive system.

III. ONLINE PARALLEL ESTIMATION OF THE MECHANICAL PARAMETERS

This section provides a new idea for attaining the online parallel estimation of the three mechanical parameters. Besides, interesting topics, such as asymptotic convergence analysis, sliding-mode chattering suppression, and Coulomb friction torque compensation, are all covered in this section.

A. Extended PMSM Mechanical Equations

Since the viscous friction torque dominates the total friction torque after starting the motor [5], we simplify (4) as follows:

$$\dot{\omega}_m = \frac{1}{J}(T_e - T_L - B\omega_m). \tag{5}$$

Here, the Coulomb friction torque is ignored to simplify our analysis. We will discuss its compensation details in Section III-E. Based on (5), several different extended PMSM mechanical motion equations can be constructed as follows:

$$\Sigma_1 : \begin{cases} \dot{\omega}_{m1} = r(T_{e1} - T_L - B\omega_{m1}) \\ \dot{r} = d_1 \end{cases} \tag{6}$$

$$\Sigma_2 : \begin{cases} \dot{\omega}_{m2} = r(T_{e2} - T_L - B\omega_{m2}) \\ \dot{B} = d_2 \end{cases} \tag{7}$$

$$\Sigma_3 : \begin{cases} \dot{\omega}_{m3} = r(T_{e3} - T_L - B\omega_{m3}) \\ \dot{T}_L = d_3 \end{cases} \tag{8}$$

where *r* = 1/*J*; $\omega_{mi} (i = 1, 2, 3)$ stands for the mechanical angular speed; $T_{ei} (i = 1, 2, 3)$ denotes the electromagnetic torque; d_1, d_2, and d_3 are the time derivatives of *r*, *B*, and T_L, respectively. In this article, these extended PMSM mechanical equations lay the groundwork for the online parallel estimation of the three mechanical parameters.

B. Designs of Novel ESMOs

Based on the ESMO methodology, this article develops three novel ESMOs to observe the states of the systems Σ_1, Σ_2, and Σ_3. In the system Σ_1, taking ω_{m1} and *r* as the observation objects, an ESMO for estimating the moment of inertia *J* can be designed as follows:

$$\text{O}_1 : \begin{cases} \dot{\hat{\omega}}_{m1} = \hat{r}(T_{e1} - \hat{T}_L - \hat{B}\hat{\omega}_{m1}) + k_1 sign(S_1) \\ \dot{\hat{r}} = P_1 \end{cases} \tag{9}$$

where $\hat{\omega}_{m1}, \hat{B}, \hat{T}_L$, and $\hat{r}$ stand for the estimated values of ω_{m1}, B, T_L, and *r*, respectively; k_1 is the switching gain; S_1 and P_1 are the sliding-mode surface and the equivalent derivative of *r*, respectively, which will be designed later.

Similarly, an ESMO for estimating the viscous friction coefficient *B* and an ESMO for determining the load torque T_L can be described as, respectively, follows:

$$\mathrm{O}_2 : \begin{cases} \dot{\hat{\omega}}_{m2} = \hat{r}(T_{e2} - \hat{T}_L - \hat{B}\hat{\omega}_{m2}) + k_2\mathrm{sign}(S_2) \\ \dot{\hat{B}} = P_2 \end{cases} \tag{10}$$

and

$$\mathrm{O}_3 : \begin{cases} \dot{\hat{\omega}}_{m3} = \hat{r}(T_{e3} - \hat{T}_L - \hat{B}\hat{\omega}_{m3}) + k_3\mathrm{sign}(S_3) \\ \dot{\hat{T}}_L = P_3 \end{cases} \tag{11}$$

where $\hat{\omega}_{m2}$ and $\hat{\omega}_{m3}$ represent the estimated values of $\omega_{\mathrm{m}2}$ and $\omega_{\mathrm{m}3}$, respectively; P_2 and P_3 stand for the equivalent derivatives of *B* and T_L, respectively; S_2 and S_3 denote the sliding-mode surfaces; both k_2 and k_3 are the switching gains. Note that P_2, P_3, S_2, and S_3 will be designed later.

In reality, it is not necessary to estimate ω_{m1}, ω_{m2}, and ω_{m3} utilizing the designed ESMOs $\mathrm{O}_1, \mathrm{O}_2$, and O_3. The mechanical angular speed can be directly measured using the encoder. The purpose of the three ESMOs is to determine the mechanical parameters T_L, J, and *B*.

Define $e_{SMO1\_1} = \hat{\omega}_{m1} - \omega_{m1}$, $e_{SMO2\_1} = \hat{\omega}_{m2} - \omega_{m2}$, $e_{SMO3\_1} = \hat{\omega}_{m3} - \omega_{m3}$, $e_{SMO1\_2} = \hat{r} - r$, $e_{SMO2\_2} = \hat{B} - B$, and $e_{SMO3\_2} = \hat{T}_L - T_L$. Subtracting (6) from (9), the error equation of the ESMO (9) can be obtained as follows:

$$\begin{cases} \dot{e}_{SMO1\_1} = R_{SMO1}e_{SMO1\_2} + F_{SMO1} + k_1\mathrm{sign}(S_1) \\ \dot{e}_{SMO1\_2} = P_1 - d_1 \end{cases} \tag{12}$$

where

$$\begin{cases} R_{SMO1} = T_{e1} - \hat{T}_L - \hat{B}\hat{\omega}_{m1} \\ F_{SMO1} = -r\hat{B}e_{SMO1\_1} - re_{SMO3\_2} - r\omega_{m1}e_{SMO2\_2}. \end{cases} \tag{13}$$

In a similar manner, we can derive the respective error equations of O_2 and O_3 as follows, respectively:

$$\begin{cases} \dot{e}_{SMO2\_1} = R_{SMO2}e_{SMO2\_2} + F_{SMO2} + k_2\mathrm{sign}(S_2) \\ \dot{e}_{SMO2\_2} = P_2 - d_2 \end{cases} \tag{14}$$

and

$$\begin{cases} \dot{e}_{SMO3\_1} = R_{SMO3}e_{SMO3\_2} + F_{SMO3} + k_3\mathrm{sign}(S_3) \\ \dot{e}_{SMO3\_2} = P_3 - d_3 \end{cases} \tag{15}$$

where

$$\begin{cases} R_{SMO2} = -\hat{r}\hat{\omega}_{m2} \\ F_{SMO2} = e_{SMO1\_2}(T_{e2} - T_L - B\omega_{m2}) \\ \qquad - \hat{r}Be_{SMO2\_1} - \hat{r}e_{SMO3\_2} \\ R_{SMO3} = -\hat{r} \\ F_{SMO3} = e_{SMO1\_2}(T_{e3} - T_L - B\omega_{m3}) \\ \qquad - \hat{r}Be_{SMO3\_1} - \hat{r}\hat{\omega}_{m3}e_{SMO2\_2}. \end{cases} \tag{16}$$

Assumption 1: The variables F_{SMO1}, R_{SMO1}, and e_{SMO1_2} are bounded and defined by $F_1^* = \sup|F_{SMO1}|$, $R_1^* = \sup|R_{SMO1}|$, and $e_1^* = \sup|e_{SMO1\_2}|$, respectively.

Theorem 1: Suppose that Assumption 1 holds for (12). The error e_{SMO1_1} and its derivative $\dot{e}_{SMO1\_1}$ in (12) will converge to zero in finite time if the sliding-mode surface S_1 is selected as $S_1 = \hat{\omega}_{m1} - \omega_{m1}$, and the switching gain k_1 is designed as $k_1 < -(R_1^*e_1^* + F_1^*)$.

Proof: Considering a Lyapunov function: $V_1 = 0.5S_1^2$.Then, the derivative of V_1 concerning time *t* can be given by

$$\dot{V}_1 = S_1 \cdot \dot{S}_1 = e_{SMO1\_1} \cdot \dot{e}_{SMO1\_1}. \tag{17}$$

Then, based on (12), we can obtain the following:

$$\begin{aligned} \dot{V}_1 &= e_{SMO1\_1}[R_{SMO1}e_{SMO1\_2} + F_{SMO1} + k_1\mathrm{sign}(e_{SMO1\_1})] \\ &\leq [R_1^*e_1^* + F_1^* + k_1]\,|e_{SMO1\_1}| \\ &= \sqrt{2}[R_1^*e_1^* + F_1^* + k_1]V_1^{\frac{1}{2}}. \end{aligned} \tag{18}$$

Choosing $k_1 < -(R_1^*e_1^* + F_1^*)$ yields

$$\dot{V}_1 = S_1 \cdot \dot{S}_1 < 0 \text{ for } S_1 \neq 0. \tag{19}$$

Therefore, the sliding mode reachable condition is satisfied. When the ESMO (9) enters into the sliding mode, the error e_{SMO1_1} and its derivative $\dot{e}_{SMO1\_1}$ can converge to zero. This completes the proof of Theorem 1.

Similarly, we assume that the variables F_{SMO2}, R_{SMO2}, e_{SMO2_2}, F_{SMO3}, R_{SMO3}, and e_{SMO3_2} are bounded and defined by $F_2^* = \sup|F_{SMO2}|$, $R_2^* = \sup|R_{SMO2}|$, $e_2^* = \sup|e_{SMO2\_2}|$, $F_3^* = \sup|F_{SMO3}|$, $R_3^* = \sup|R_{SMO3}|$, and $e_3^* = \sup|e_{SMO3\_2}|$, respectively. Then, one can conclude that the errors (e_{SMO2_1}, e_{SMO3_1}) and their derivatives ($\dot{e}_{SMO2\_1}$, $\dot{e}_{SMO3\_1}$) can converge to zero in finite time if S_2, k_2, S_3, and k_3 are designed as $S_2 = \hat{\omega}_{m2} - \omega_{m2}$, $k_2 < -(R_2^*e_2^* + F_2^*)$, $S_3 = \hat{\omega}_{m3} - \omega_{m3}$, and $k_3 < -(R_3^*e_3^* + F_3^*)$, respectively. Here, the related proofs are omitted since they are incredibly similar to the proof of Theorem 1.

Theorem 2: The estimation errors e_{SMO1_2}, e_{SMO2_2}, and e_{SMO3_2} will tend to zero asymptotically if P_1, P_2, and P_3 are designed, respectively, as follows:

$$P_1 = q_1(T_{e1} - \hat{T}_L - \hat{B}\hat{\omega}_{m1})k_1\mathrm{sign}(\hat{\omega}_{m1} - \omega_{m1}) \tag{20}$$

$$P_2 = -q_2\hat{r}\hat{\omega}_{m2}k_2\mathrm{sign}(\hat{\omega}_{m2} - \omega_{m2}) \tag{21}$$

$$P_3 = -q_3\hat{r}k_3\mathrm{sign}(\hat{\omega}_{m3} - \omega_{m3}) \tag{22}$$

where $q_1 > 0$, $q_2 > 0$, and $q_3 > 0$. Note that the items $q_1(T_{e1} - \hat{T}_L - \hat{B}\hat{\omega}_{m1})$, $-q_2\hat{r}\hat{\omega}_{m2}$, and $-q_3\hat{r}$ are the corresponding feedback gains. Here, we define $g_1 = q_1(T_{e1} - \hat{T}_L - \hat{B}\hat{\omega}_{m1})$, $g_2 = -q_2\hat{r}\hat{\omega}_{m2}$, and $g_3 = -q_3\hat{r}$.

Proof: From the preceding analysis, we can know that the equations $e_{SMO1\_1} = \dot{e}_{SMO1\_1} = 0$, $e_{SMO2\_1} = \dot{e}_{SMO2\_1} = 0$, and $e_{SMO3\_1} = \dot{e}_{SMO3\_1} = 0$ hold when the sliding modes are reached. Therefore, we have the following:

$$\begin{cases} R_{SMO1}e_{SMO1\_2} + F'_{SMO1} + k_1\mathrm{sign}(\hat{\omega}_{m1} - \omega_{m1}) = 0 \\ \dot{e}_{SMO1\_2} = P_1 - d_1 \end{cases} \tag{23}$$

$$\begin{cases} R_{SMO2}e_{SMO2\_2} + F_{SMO2}^{'} + k_2\mathrm{sign}(\hat{\omega}_{m2} - \omega_{m2}) = 0 \\ \dot{e}_{SMO2\_2} = P_2 - d_2 \end{cases} \tag{24}$$

$$\begin{cases} R_{SMO3}e_{SMO3\_2} + F_{SMO3}^{'} + k_3\mathrm{sign}(\hat{\omega}_{m3} - \omega_{m3}) = 0 \\ \dot{e}_{SMO3\_2} = P_3 - d_3 \end{cases} \tag{25}$$

where

$$\begin{cases} F_{SMO1}^{'} = -re_{SMO3\_2} - r\omega_{m1}e_{SMO2\_2} \\ F_{SMO2}^{'} = e_{SMO1\_2}(T_{e2} - T_L - B\omega_{m2}) - \hat{r}e_{SMO3\_2} \\ F_{SMO3}^{'} = e_{SMO1\_2}(T_{e3} - T_L - B\omega_{m3}) - \hat{r}\hat{\omega}_{m3}e_{SMO2\_2}. \end{cases} \tag{26}$$

Integrating (20) into (23) leads to

$$\dot{e}_{SMO1\_2} + g_1R_{SMO1}e_{SMO1\_2} + g_1F_{SMO1}^{'} + d_1 = 0. \tag{27}$$

Similarly, we can obtain the following:

$$\dot{e}_{SMO2\_2} + g_2R_{SMO2}e_{SMO2\_2} + g_2F_{SMO2}^{'} + d_2 = 0 \tag{28}$$

$$\dot{e}_{SMO3\_2} + g_3R_{SMO3}e_{SMO3\_2} + g_3F_{SMO3}^{'} + d_3 = 0. \tag{29}$$

Generally, the change frequency of the mechanical parameters is far less than the switching frequency of the PMSM-based drive system. Therefore, it is considered that the three concerned parameters are constants within an extremely short time, which means $d_1 = d_2 = d_3 = 0$ under such condition. Then, we conclude the following:

$$\dot{e}_{SMO1\_2} + g_1R_{SMO1}e_{SMO1\_2} + g_1F_{SMO1}^{'} = 0 \tag{30}$$

$$\dot{e}_{SMO2\_2} + g_2R_{SMO2}e_{SMO2\_2} + g_2F_{SMO2}^{'} = 0 \tag{31}$$

$$\dot{e}_{SMO3\_2} + g_3R_{SMO3}e_{SMO3\_2} + g_3F_{SMO3}^{'} = 0. \tag{32}$$

When $g_1F_{SMO1}^{'}$, $g_2F_{SMO2}^{'}$, and $g_3F_{SMO3}^{'}$ are controlled near zero, the parameter estimation errors are exponentially convergent. The reasons are as follows: If $g_1F_{SMO1}^{'} \approx 0$, $g_2F_{SMO2}^{'} \approx 0$, and $g_3F_{SMO3}^{'} \approx 0$ hold, we can derive the analytical expressions of (30), (31), and (32) as follows:

$$e_{SMO1\_2} = C_1e^{-\int(g_1R_{SMO1})\mathrm{d}t} \tag{33}$$

$$e_{SMO2\_2} = C_2e^{-\int(g_2R_{SMO2})\mathrm{d}t} \tag{34}$$

$$e_{SMO3\_2} = C_3e^{-\int(g_3R_{SMO3})\mathrm{d}t} \tag{35}$$

where C_1, C_2, and C_3 are constants. We notice the following:

$$g_1R_{SMO1} > 0 \text{ for } (T_{e1} - \hat{T}_L - \hat{B}\hat{\omega}_{m1}) \neq 0 \tag{36}$$

$$g_2R_{SMO2} > 0 \text{ for } \hat{r}\hat{\omega}_{m2} \neq 0 \tag{37}$$

$$g_3R_{SMO3} > 0 \text{ for } \hat{r} \neq 0. \tag{38}$$

Hence, based on the analytic expressions, we can conclude that the estimation errors e_{SMO1_2}, e_{SMO2_2}, and e_{SMO3_2} tend to zero exponentially with time t. To ensure that $g_1F_{SMO1}^{'} \approx 0$, $g_2F_{SMO2}^{'} \approx 0$, and $g_3F_{SMO3}^{'} \approx 0$ are satisfied, the values of q_1, q_2, and q_3 are crucial. Specifically, the values of $g_1F_{SMO1}^{'}, g_2F_{SMO2}^{'}$, and $g_3F_{SMO3}^{'}$ should be guaranteed to be small enough. This purpose can be achieved with appropriate q_1, q_2, and q_3. Additionally, it can be found from (33)–(35) that the values of q_1, q_2, and q_3 are associated with the convergence rate. By analyzing further, it follows that a smaller $q_i(i = 1, 2, 3)$ means a slower convergence rate and higher estimation accuracy. With the abovementioned analysis, Theorem 2 is proved.

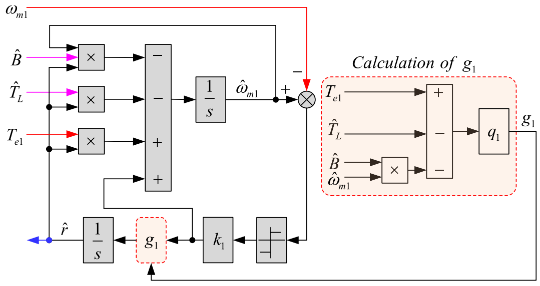

Fig. 2. Schematic block diagram of the ESMO used for estimating J.

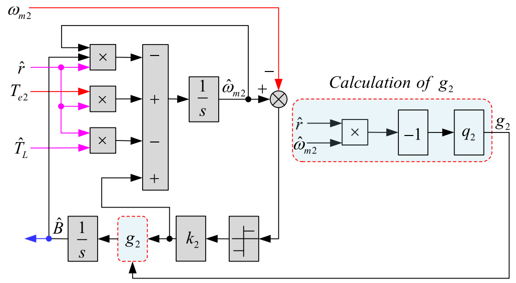

Fig. 3. Schematic block diagram of the ESMO used for estimating B.

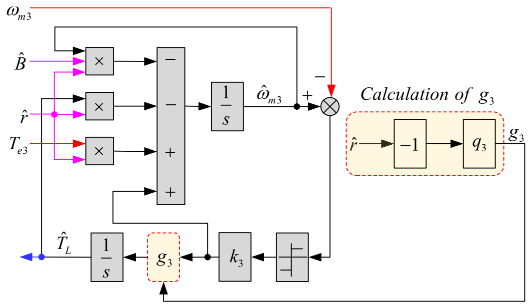

Fig. 4. Schematic block diagram of the ESMO used for estimating T_L.

From Theorem 2, it can be known that the knowledge of the mechanical parameters is exploited to design the equivalent derivatives, and the feedback gains are time-varying. These are the significant characteristics of the proposed ESMOs. It should be noted that, in order to attain the online parallel estimation of the three concerned parameters subsequently, the equivalent derivatives presented here are devised by directly using the estimates of these parameters. From the abovementioned analysis, we can gain the principle block diagrams of the ESMOs O_1, O_2, and O_3, as shown in Figs. 2–4, respectively.

Remark 1: In the proof of Theorem 2, it is noticed that the parameter estimation errors tend to zero exponentially over time without resorting to any initial conditions. This implies that the estimates of the three parameters can asymptotically approach the real values from different arbitrary initial values.

C. Chattering Suppression Analysis

It is well-recognized that the sliding-mode chattering is a crucial technical problem, which impairs the desired performance of the SMO. Therefore, to achieve better estimation performance of the mechanical parameters, the sliding-mode chattering must be mitigated.

First, we define the sliding-mode chattering signals in the estimation parameters $\hat{J}$, $\hat{B}$, and $\hat{T}_L$ as A_1, A_2, and A_3, respectively. Next, we take the chattering signal A_1 as an example to analyze the chattering suppression. When the ESMO (9) reaches the sliding mode, the error equation (12) can be rewritten as follows:

$$\begin{cases} A_1 = R_{SMO1}e_{SMO1\_2} + F'_{SMO1} + k_1\mathrm{sign}(\hat{\omega}_{m1} - \omega_{m1}) \\ \dot{e}_{SMO1\_2} = P_1 - d_1. \end{cases} \tag{39}$$

The combination of (20) and (39) leads to

$$\begin{cases} A_1 = R_{SMO1}e_{SMO1\_2} + F'_{SMO1} + k_1\mathrm{sign}(\hat{\omega}_{m1} - \omega_{m1}) \\ \dot{e}_{SMO1\_2} = q_1(T_{e1} - \hat{T}_L - \hat{B}\hat{\omega}_{m1})k_1\mathrm{sign}(\hat{\omega}_{m1} - \omega_{m1}) - d_1. \end{cases} \tag{40}$$

As a result, the error equation of the moment of inertia with the chattering signal A_1 can be formulated as follows:

$$\dot{e}_{SMO1\_2} + g_1 R_{SMO1}e_{SMO1\_2} + g_1 F'_{SMO1} + d_1 - g_1 A_1 = 0. \tag{41}$$

Then, we can obtain the transfer function of (41), i.e.,

$$e_{SMO1\_2} = \frac{\omega_{f1}}{\omega_{f1} + s} \cdot \frac{A_1}{R_{SMO1}} - \frac{\omega_{f1}}{\omega_{f1} + s} \cdot \frac{g_1 F'_{SMO1} + d_1}{g_1 R_{SMO1}} \tag{42}$$

where $\omega_{f1} = g_1 R_{SMO1} \geq 0$. Thereupon, one can conclude that the sliding-mode chattering signal A_1 is restrained by an LPF with cutoff frequency ω_{f1}. Therefore, designing P_1 is equivalent to indirectly designing the cutoff frequency of an LPF, which means that the proposed ESMO (9) possesses an inherent property for restraining the chattering. That is to say, extra chattering suppression is not needed.

With a similar manner, we can derive:

$$e_{SMO2\_2} = \frac{\omega_{f2}}{\omega_{f2} + s} \cdot \frac{A_2}{R_{SMO2}} - \frac{\omega_{f2}}{\omega_{f2} + s} \cdot \frac{g_2 F'_{SMO2} + d_2}{g_2 R_{SMO2}} \tag{43}$$

$$e_{SMO3\_2} = \frac{\omega_{f3}}{\omega_{f3} + s} \cdot \frac{A_3}{R_{SMO3}} - \frac{\omega_{f3}}{\omega_{f3} + s} \cdot \frac{g_3 F'_{SMO3} + d_3}{g_3 R_{SMO3}} \tag{44}$$

where $\omega_{f2} = g_2 R_{SMO2}$ and $\omega_{f3} = g_3 R_{SMO3}$. From (43) and (44), we can find that the chattering signals A_2 and A_3 can be suppressed by the LPF with cutoff frequency ω_{f2} and the LPF with cutoff frequency ω_{f3}, respectively.

According to the abovementioned analysis, we can know the values of $q_i (i = 1, 2, 3)$ are also associated with the chattering suppression. Smaller $q_i (i = 1, 2, 3)$ will better suppress the chattering, and however, the dynamic performance may be impaired. This will be discussed in detail in Section IV.

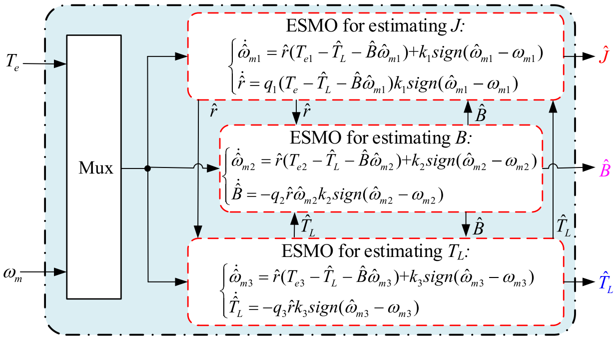

Fig. 5. Schematic block diagram of the proposed network.

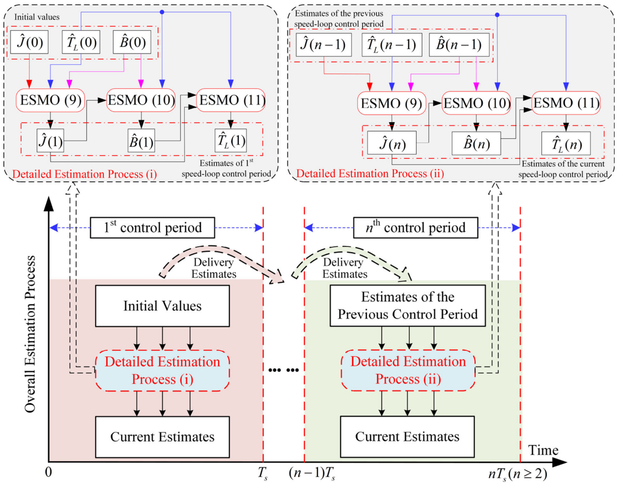

Fig. 6. Parameter estimation process of the proposed network.

D. Network of Interconnected ESMOs

To accomplish the online parallel estimation of the three mechanical parameters, we develop an interconnected-observer-based network using the proposed ESMOs. The block diagram of the proposed network is demonstrated in Fig. 5. In this network, the three ESMOs provide updates to each other in real time and operate in parallel. From Fig. 5, we can see that the developed network has three outputs. The chattering in these outputs can be well suppressed due to the inherent LPF property. Notably, this property implies that high switching gains are allowed, without aggravating the chattering. (Since these switching gains in the proposed ESMOs are negative, the previous analysis means that the absolute values of these gains can be selected as large values.) When using the presented network, the detailed parameter estimation process is shown in Fig. 6, where T_s is the speed-loop control period.

To ensure the stability of the developed network, we consider a new Lyapunov function:

$$V = \frac{1}{2}S_1^2 + \frac{1}{2}S_2^2 + \frac{1}{2}S_3^2. \tag{45}$$

Then, we have the following:

$$\begin{aligned}\dot{V} &= S_1\dot{S}_1 + S_2\dot{S}_2 + S_2\dot{S}_2\\ &= e_{SMO1\_1}\cdot\dot{e}_{SMO1\_1} + e_{SMO2\_1}\cdot\dot{e}_{SMO2\_1}\\ &\quad + e_{SMO3\_1}\cdot\dot{e}_{SMO3\_1}\\ &\le [|R_{SMO1}e_{SMO1\_2} + F_{SMO1}| + k_1]\,|e_{SMO1\_1}|\\ &\quad + [|R_{SMO2}e_{SMO2\_2} + F_{SMO2}| + k_2]\,|e_{SMO2\_1}|\\ &\quad + [|R_{SMO3}e_{SMO3\_2} + F_{SMO3}| + k_3]\,|e_{SMO3\_1}|\\ &\le [R_1^*e_1^* + F_1^* + k_1]\,|e_{SMO1\_1}|\\ &\quad + [R_2^*e_2^* + F_2^* + k_2]\,|e_{SMO2\_1}|\\ &\quad + [R_3^*e_3^* + F_3^* + k_3]\,|e_{SMO3\_1}|.\end{aligned} \tag{46}$$

According to the discussions concerning the values of $k_i(i = 1, 2, 3)$ in Section III-B, we can know that $\dot{V} < 0$ holds. Hence, the global stability of the network can be guaranteed.

E. Coulomb Friction Torque Compensation

During the design of the ESMOs used for estimating the three mechanical parameters, we ignored the Coulomb friction torque to simplify the analysis. However, the accuracy of the mechanical-motion-equation-based estimation methods is bound to be affected by the correctness of the equation. The neglect of the Coulomb friction torque will unavoidably degrade the estimation accuracy of the proposed network. Especially in some applications with a large Coulomb friction coefficient, this problem will likely become more remarkable. Hence, the Coulomb friction torque should be compensated for in the network to achieve higher estimation accuracy.

Remark 2: It can be seen from (4) that ignoring any term of this equation is bound to have a negative impact on the parameter estimation, resulting in deteriorative estimation accuracy. Therefore, the mechanical-motion-equation-based estimation method should consider a more accurate motion model as much as possible to acquire reliable estimation accuracy. This is an aspect neglected by the current online parallel estimation methods.

Remark 3: In our presented network, the three ESMOs are all developed based on the mechanical motion equation (5). Here, the detailed adverse effects of Coulomb friction torque on the proposed network are analyzed in terms of this equation. It is well-recognized that the inertia identification is valid only when the rotor speed changes, and has no meaning at the steady state. At the transient state, it can be derived from (5) that the equation $J = (T_e - T_L - B\omega_m)/\dot{\omega}_m$ holds. Due to the extremely large acceleration of the PMSM system in the transient state, the Coulomb friction torque that exists in the numerator of this equation can be ignored compared with the large denominator. Nevertheless, when the acceleration is small or when the Coulomb friction torque is quite large, the inertia estimation result will be implicated. Assuming that the inertia estimation result is not affected, the electromagnetic torque T_e and the inertia torque $J\dot{\omega}_m$ can be combined into one item, i.e., $T_e' = T_e - J\dot{\omega}_m$. Thus, we have: $T_e' = T_L + B\omega_m$. By comparing with the motion equation containing Coulomb friction torque ($T_e' = T_L + B\omega_m + C\text{sign}(\omega_m)$), it can be seen that the estimation accuracy of T_L and B will inevitably be destroyed if the Coulomb friction torque is not removed. Additionally, it should be noted that under the bidirectional speed, the estimation of B will suffer from noticeable deterioration since the viscous and Coulomb friction torques are of the same frequency [33].

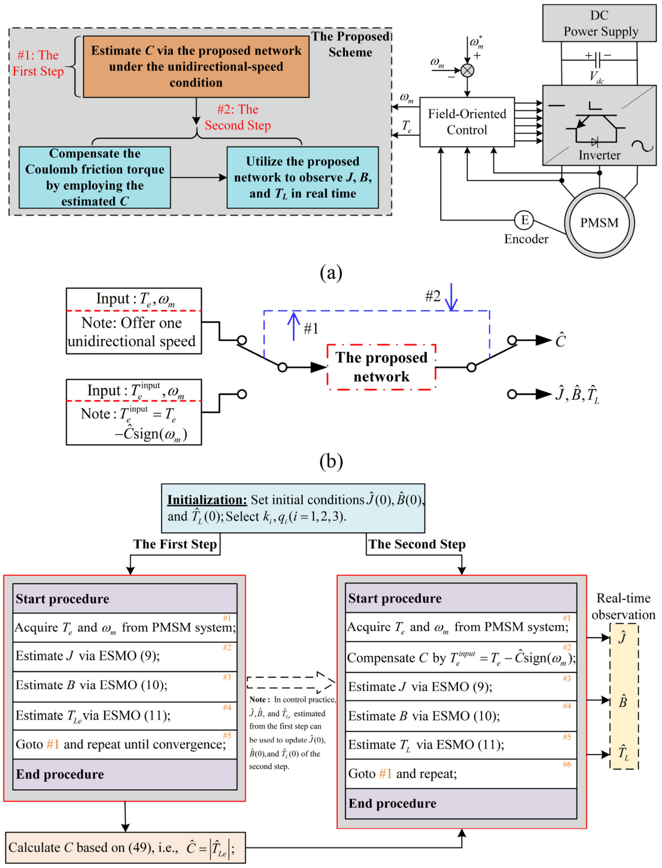

Fig. 7. Online parallel estimation scheme with a two-step mechanism. (a) Components of our scheme. (b) Relationship between the two steps. (c) Flowchart of our scheme.

The Coulomb friction torque is dependent on the rotation direction. Hence, in a practical application, it is difficult to directly estimate it in an online manner due to its rapid vibrations. The effective approach for online acquiring the Coulomb friction torque is to identify the Coulomb friction coefficient in advance and then calculate it in real time according to the motor's rotation direction. Generally, the system commissioning process is supposed to be carried out after the PMSM system is equipped into an actual application system [32]. In this process, the load torque is usually considered zero. In order to ensure that the three concerned parameters can be accurately identified during the task, it is necessary to acquire the value of the Coulomb friction coefficient during the system commissioning process.

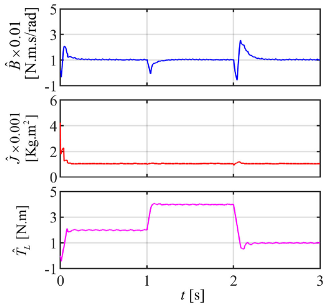

Fig. 8. Simulation results at Case 1.

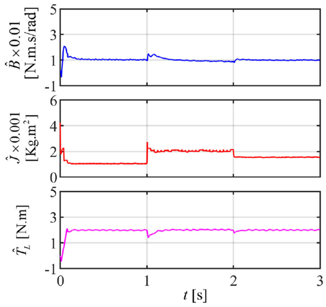

Fig. 9. Simulation results at Case 2.

TABLE I
SIMULATION SETUP AND CASES

Content	Description				
Simulation setup	Speed command $s^* = speed(600,12.5) - 200$; Parameters of PMSM: $L_d = L_q$=1.81 mH, $P_n = 5$, R_m= 0.39 Ω, ψ_f = 0.1313 Wb; The switching frequency of the inverter: 5 kHz; Initial values: $\hat{J}(0) = 4\times 1.061\times 10^{-3}, \hat{T}_L(0) = 0, \hat{B}(0) = 0.002$.				
Simulation Cases ($C = 0$)	Case 1	Refe. B = 0.01; Refe. J = 1.061×10^{-3} ;	$t \le 1$ s	$1 < t \le 2$ s	$2 < t \le 3$ s
			Refe. $T_L = 2$	Refe. $T_L = 4$	Refe. $T_L = 1$
	Case 2	Refe. B = 0.01; Refe. T_L = 2;	$t \le 1$ s	$1 < t \le 2$ s	$2 < t \le 3$ s
			Refe. J = 1.061×10^{-3}	Refe. J = 2.122×10^{-3}	Refe. J = 1.592×10^{-3}
	Case 3	Refe. T_L = 2; Refe. J = 1.061×10^{-3} ;	$t \le 1$ s	$1 < t \le 2$ s	$2 < t \le 3$ s
			Refe. B = 0.01	Refe. B = 0.03	Refe. B= 0.02
	Case 4	Refe. $[T_L, J, B] = \begin{cases} [2, 1.061\times 10^{-3}, 0.01] & (t \le 1 \text{ s}) \\ [4, 2.122\times 10^{-3}, 0.03] & (1 < t \le 2 \text{ s}) \\ [1, 1.592\times 10^{-3}, 0.02] & (2 < t \le 3 \text{ s}) \end{cases}$			
	Case 5	Refe. J, B, and T_L stay aligned with Case 1. The two inputs of the network, i.e., ω_m and T_e , are slightly contaminated by noise.			
	Case 6	Refe. J, B, and T_L stay aligned with Case 1. The two inputs of the network, i.e., ω_m and T_e , are severely contaminated by noise.			

Note: "Refe." represents "Referenced," and the units of J, B, and T_L are Kg.m^2, N.m.s/rad, and N.m, respectively.

Based on the developed network, this purpose can be achieved. The detailed description is as follows.

We notice that the Coulomb friction torque can be transformed into the constant load torque, provided that one unidirectional speed command is utilized. Thus, when a unidirectional time-varying speed is used to drive the motor during the commissioning process, (4) can be converted to

$$J\dot{\omega}_m = T_e - T_{Le} - B\omega_m \tag{47}$$

where T_{Le} is regarded as the equivalent load torque caused by the Coulomb friction torque, which is expressed as follows:

$$T_{Le} = \begin{cases} +C, (\omega_m > 0) \\ 0, (\omega_m = 0) \\ -C, (\omega_m < 0). \end{cases} \tag{48}$$

It is noted that the three unknown parameters in (47), i.e., J, B, and T_{Le}, can be directly estimated using the presented network. After the identified result of the equivalent load torque is determined, the estimated value of the Coulomb friction coefficient can be calculated as follows:

$$\hat{C} = \left|\hat{T}_{Le}\right| \tag{49}$$

where $\hat{T}_{Le}$ is the estimated value of T_{Le}.

Based on (49), the Coulomb friction torque can be computed in real time. Therefore, the compensation for the Coulomb friction torque is able to be achieved. To serve this purpose, the electromagnetic torque input to the network is designed as follows:

$$T_e^{\text{input}} = T_e - \hat{C}\text{sign}(\omega_m). \tag{50}$$

When utilizing the network to estimate the three concerned parameters, (50) is used to counteract the adverse effect of Coulomb friction torque, thus, laying the groundwork for achieving accurate estimation.

F. Online Parallel Estimation Scheme Based on a Two-Step Mechanism

In the light of the abovementioned analyses, an online parallel estimation scheme with a two-step mechanism is proposed. Fig. 7 exhibits its detailed components, flowchart, and the relationship between the two steps. Note that the first step is used during the system commissioning process, while the second step is utilized during the task. In addition, it is noted that the two steps use the same network, i.e., the related parameter configurations of the network remain unchanged in the two steps. By utilizing this relevance between the online parallel estimation of the three concerned parameters and the identification of C, we can easily attain the accurate observation of the three mechanical parameters.

In the engineering practice, the parameter adjustment of the developed scheme can be conducted in accordance with the analyses in Section III-B and III-C. The parameters to be adjusted include $\hat{J}(0), \hat{B}(0), \hat{T}_L(0)$, $k_i (i = 1, 2, 3)$, and $q_i (i = 1, 2, 3)$. Based on the preceding analyses, the adjustment guidelines can be concisely summarized below.

1) $\hat{J}(0), \hat{B}(0), \hat{T}_L(0)$ can be set with arbitrary values.
2) $k_i (i = 1, 2, 3)$ is supposed to be selected as large as possible to establish the sliding-mode reachable condition

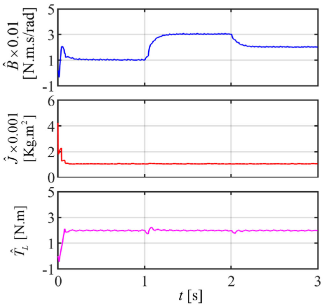

Fig. 10. Simulation results at Case 3.

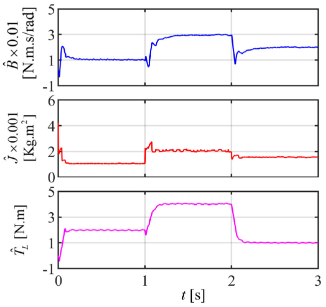

Fig. 11. Simulation results at Case 4.

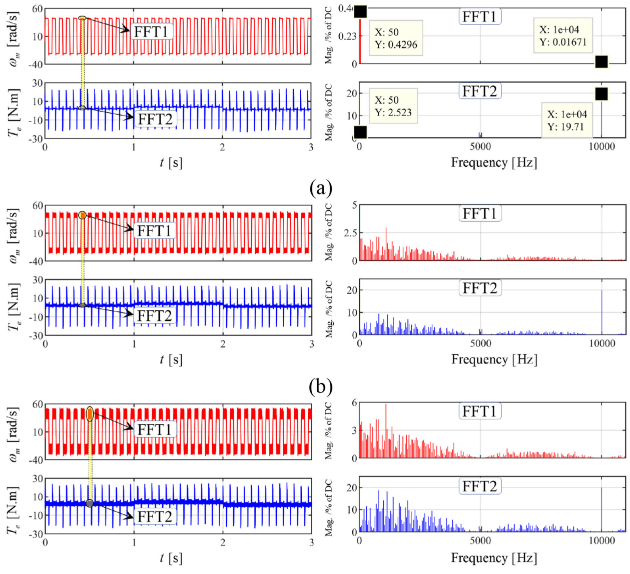

(a)

(b)

(c)

Fig. 12. Noise components in ω_m and T_e. (a) ω_m and T_e contaminated by 50-Hz low-frequency noise and high-frequency switching noise. (b) ω_m and T_e contaminated by 50-Hz low-frequency noise, high-frequency switching noise, and measurement noise (corresponding to Case 5). (c) Increase the amplitude of measurement noise on the basis of Case 5 (corresponding to Case 6).

and enable the network in both steps to be globally stable. (Note that due to the inherent LPF property, a large $k_i(i = 1, 2, 3)$ is permissive.)

3) Small $q_i(i = 1, 2, 3)$ is advantageous for weakening chattering and guaranteeing accuracy, but $q_i(i = 1, 2, 3)$ cannot be chosen too small to seek for fast convergence rates.

Remark 4: In the first step, by using only one speed, the viscous and Coulomb friction coefficients and the system inertia can be estimated simultaneously. This function is the same as that of the latest method proposed in [33]. The difference is that our scheme can also identify time-varying mechanical parameters, while the method offered in [33] cannot serve this purpose due to the fact that the time-varying parameters will cause unstable estimation. It is noted that if the system inertia and the viscous friction coefficient do not require to be observed online during the task, the estimates of these two parameters in the first step can be straight away utilized in the second one. In this way, the network can be changed to a load torque observer. The abovementioned analysis means that the presented scheme is adaptable for different task requirements.

IV. SIMULATION AND EXPERIMENTAL EXAMPLES

A. Simulation Examples

In order to assess the performance of the developed scheme, simulation studies are conducted using MATLAB/Simulink. For the simulations, the parameters of the network are selected as $k_1 = -4000, g_1 = 1.5(T_{e1} - \hat{T}_L - \hat{B}\omega_m), k_2 = -1000, g_2 = -2\times 10^{-8}\hat{r}\hat{\omega}_{m2}, k_3 = -1000,$ and $g_3 = -4\times 10^{-5}\hat{r}$. Additionally, the square-wave speed command is chosen in order to simulate the frequent speed changes in actual PMSM systems:

$$s^* = \mathrm{speed}(\omega, f) = \begin{cases} \omega, [t\cdot f - \mathrm{floor}(t\cdot f)] \le 0.5 \\ 0, \text{ other} \end{cases} \tag{51}$$

where ω and f are the amplitude and frequency of the square-wave speed command, respectively; "$\mathrm{floor}(t\cdot f)$" stands for the greatest integer less than or equal to $t\cdot f$. Note that the units of ω and f are r/min and Hz, respectively.

To comprehensively test the online identification performance of the proposed scheme, we only focus on the second step in the simulations. First, this article investigated six cases in the simulation, as described in Table I. Figs. 8–11 give the simulation results of the developed scheme under cases 1–4. As can be seen from there, whether all three mechanical parameters are time-varying or only one of them is time-varying, the proposed method can estimate these parameters quickly and accurately with low sliding-mode chattering (the estimates of the three mechanical parameters are virtually error-free).

In cases 5 and 6, the influence of noise on the proposed scheme is taken into consideration. It can be known from Section III that the proposed scheme requires real-time rotor speed ω_m and electromagnetic torque T_e. It is worth noting that ω_m and T_e are easily contaminated by noise. In order to simulate this situation, we consider the common noises in the PMSM system, such as 50-Hz low-frequency noise, high-frequency switching noise, and measurement noise. Note that the measurement noise is simulated by the random number. Fig. 12 shows the real-time rotor speed and electromagnetic torque information corresponding to the simulations under Cases 5 and 6. The Fourier analyses in Fig. 12 manifest that the abovementioned noises are present. Figs. 13 and 14 give the estimation results of

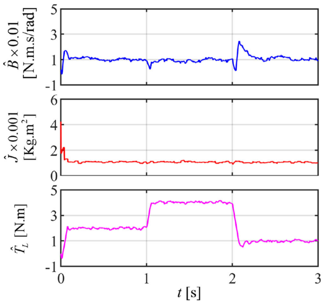

Fig. 13. Simulation results at Case 5.

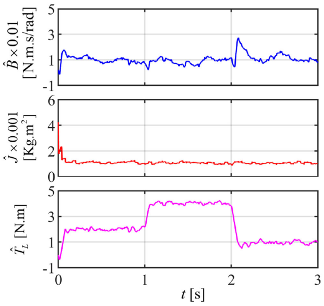

Fig. 14. Simulation results at Case 6.

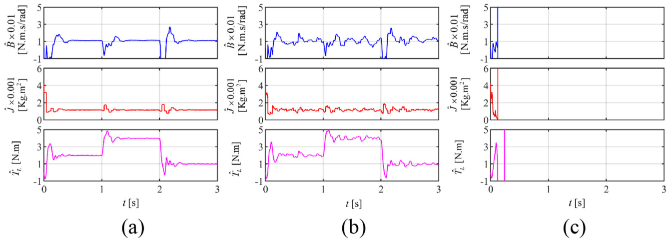

Fig. 15. Simulation results for the scheme proposed in [24]. (a) At Case 1. (b) At Case 5. (c) At Case 6.

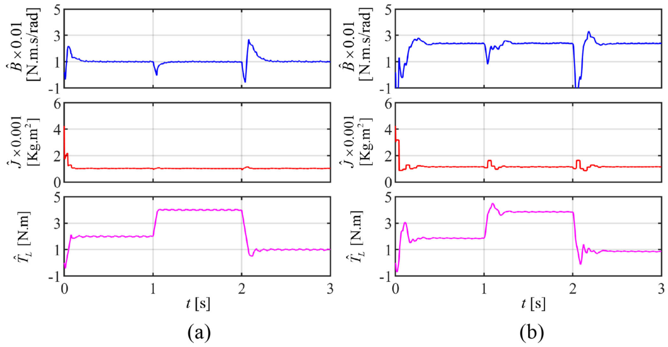

Fig. 16. Comparison between our scheme and the scheme presented in [24] under $C\neq0$. (a) Our scheme. (b) Scheme proposed in [24].

TABLE II
ESTIMATION ERRORS WHEN $t \in [2, 3]$

Tests	Error of $\hat{B}$	Error of $\hat{T}_L$	Error of $\hat{J}$
Fig. 15(a)	7.11%	≈ 0	8.58%
Fig. 16(a)	≈ 0	≈ 0	≈ 0
Fig. 16(b)	141%	12.9%	11.36%

the proposed scheme under cases 5 and 6, respectively. It can be observed from Fig. 13 that the identification results of the three mechanical parameters can converge to the given values quickly and accurately in the presence of noise. Even when severe noise contamination exists, the estimation values can still converge to the vicinities of the reference values, as shown in Fig. 14.

Together, the abovementioned simulation results indicate that the presented scheme can accurately track the three mechanical parameters in real time and has strong robustness against noise. In order to further demonstrate the antinoise superiority of the proposed scheme, the method proposed in [24] is used for comparison. In the simulations, its related parameters are set as $k_1 = 30$, $k_2 = -3$, $k_J = 0.00002$, $k_B = 0.04$. Fig. 15 gives the simulation results of this scheme, where Fig. 15(a)–(c) is obtained under case 1, case 5, and case 6, respectively. As can be seen from Fig. 15(a), this method can also track the three mechanical parameters accurately in the absence of noise. However, when the system is contaminated by noise, this method's identification results begin to fluctuate significantly and even to be nonconvergent, as displayed in Fig. 15(b) and (c).

It is noted that C is set to zero in the abovementioned simulation cases. Under $C \neq 0$, the simulation concerning the proposed scheme is also conducted. In the corresponding simulation, C is set to 0.4, and other simulation settings coincide with Case 1. Additionally, the Coulomb friction torque's compensation value is calculated by directly using the real value of C, i.e., $T_e^{\text{input}} = T_e - 0.4\text{sign}(\omega_m)$. Fig. 16(a) exhibits the proposed scheme's estimation results. From there, it can be observed that the estimates of the three concerned parameters converge to the correct results quickly. For comparison, the estimation scheme that ignores the Coulomb friction torque, i.e., [24], is simulated at $C = 0.4$. Fig. 16(b) gives the corresponding simulation results, which demonstrate that the estimation of the three mechanical parameters significantly suffers from deterioration compared with the results at $C = 0$ [see Fig. 15(a)]. The estimation errors of the Figs. 15(a) and 16 are summarized in Table II. Based on the abovementioned analysis, we can conclude that the Coulomb friction torque is supposed to be compensated to acquire the reliable estimation of the three mechanical parameters.

Fig. 17 demonstrates the simulation results with different C values when using the developed scheme, and meanwhile, the results with and without Coulomb friction torque compensation are compared. Note that other related simulation settings are consistent with Case 1, and the compensation value is calculated by directly using the real value of C. The estimation errors corresponding to Fig. 17(b) are listed in Table III. Both Fig. 17 and Table III show that before the Coulomb friction torque compensation, the estimation accuracy of the viscous friction coefficient suffers from the severest deterioration. This is because the Coulomb and viscous friction torques are indistinguishable due to the fact that they are of the same frequency under a bidirectional-speed condition. The phenomenon reported above

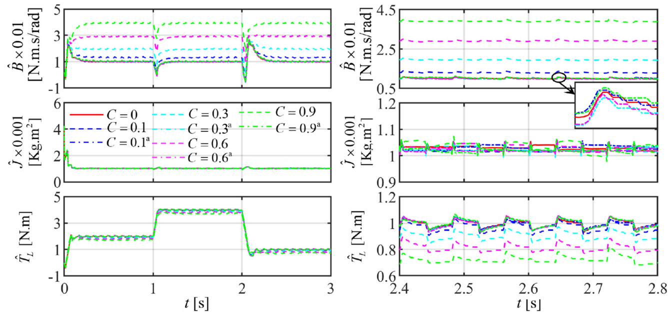

(a) (b)

Fig. 17. Influence of Coulomb friction torque on the identification of the parameters J, B, and T_L. (a) Comparison of the estimation results. (b) Enlarged view of (a) when $t \in [2, 3]$.

TABLE III
ESTIMATION ERRORS CORRESPONDING TO Fig. 17(b)

Parameters	Error of $\hat{B}$	Error of $\hat{T}_L$	Error of $\hat{J}$
C = 0	≈ 0	≈ 0	≈ 0
C = 0.1	37.1%	3.1%	≈ 0
C = 0.1[a]	≈ 0	≈ 0	≈ 0
C = 0.3	98.2%	8.7%	≈ 0
C = 0.3[a]	≈ 0	≈ 0	≈ 0
C = 0.6	194.8%	20.2%	≈ 0
C = 0.6[a]	≈ 0	≈ 0	≈ 0
C = 0.9	288.4%	29.2%	≈ 0
C = 0.9[a]	≈ 0	≈ 0	≈ 0

[a] The Coulomb friction torque is compensated online.

will become more pronounced with the increasing Coulomb friction coefficient. In addition, before compensating the Coulomb friction torque, the estimation of the load torque is also subject to some degree of damage, as displayed in Fig. 17(b). Moreover, it is supposed to be pointed out that the influence of Coulomb friction torque on identifying the system inertia is almost negligible, which can be seen from Fig. 17(b). This seems to contradict the analysis in Remark 2. Actually, this phenomenon results from the large acceleration, as explained by Remark 3. Overall, all the abovementioned phenomena are in good agreement with the analyses in Section III-E. Through the abovementioned simulations and comparisons, the effectiveness of our proposed scheme is further tested.

The inherent torque ripples in the PMSM drives deteriorate the control performance and result in the speed ripples [34], [35]. In order to evaluate the influence of torque and speed ripples on the presented scheme, the corresponding simulation study is performed based on Case 1. Usually, the first harmonic is the dominant component in the torque ripples [34]. Thus, to produce and simulate torque and speed ripples, we utilize the harmonic model introduced in [34] to generate the first harmonic signal and then superimpose it on the q-axis feedback current i_q. Here, the harmonic signal is set as $i_{\text{ripple}} = 1.5\cos(5\theta) + 0.4\sin(5\theta)$, where θ is the rotor position. Fig. 18 shows the corresponding estimation results. From there, we can observe that these results are almost consistent with those in Fig. 8. Thus, it can be concluded that the influence of the torque and speed ripples on our presented scheme is almost negligible.

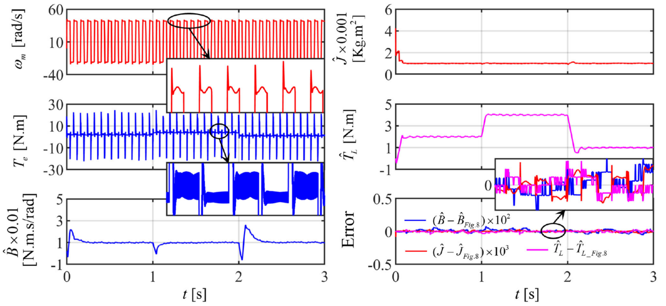

Fig. 18. Influence of torque and speed ripples on the presented scheme.

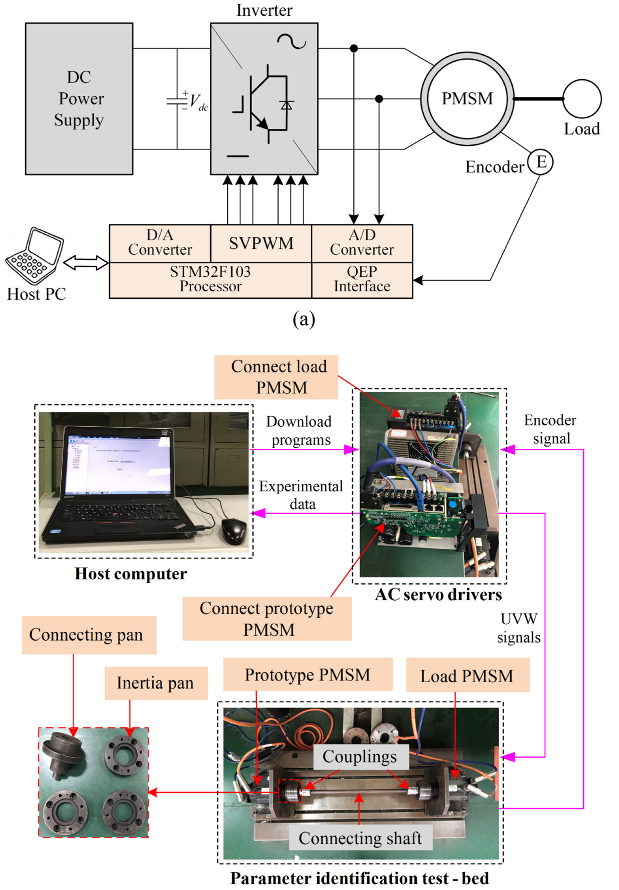

(b)

Fig. 19. Experimental platform. (a) Configuration of the test bench. (b) Photograph of the test bench.

B. Experimental Examples

To further test the performance of the presented method, an experimental investigation is conducted based on the built experimental platform shown in Fig. 19. Note that the control strategy is based on field-oriented control with $i_d^* = 0$, as displayed in Fig. 1. The built experimental platform mainly consists of the following three parts: 1) two STM32F103-based ac servo

TABLE IV
SPECIFICATION OF THE EXPERIMENTAL PLATFORM

Parameters	Value
Rated speed	2000 r/min
Rated current	6.5 A
Rated torque	6.4 N.m
Rotor inertia	1.061×10^{-3} Kg.m^{2}
Nominal stator resistance	0.39 Ω
Nominal phase inductance	1.81 mH
Number of pole pairs	5
Nominal value of inertia of a connecting pan	1.088×10^{-3} Kg.m^{2}
Nominal value of inertia of a pair of couplings	0.08×10^{-3} Kg.m^{2}
Nominal value of inertia of the connecting shaft	6.321×10^{-5} Kg.m^{2}
Nominal value of inertia of an inertia pan	1.108×10^{-3} Kg.m^{2}

Note: Nominal values are obtained by measurement and/or calculation.

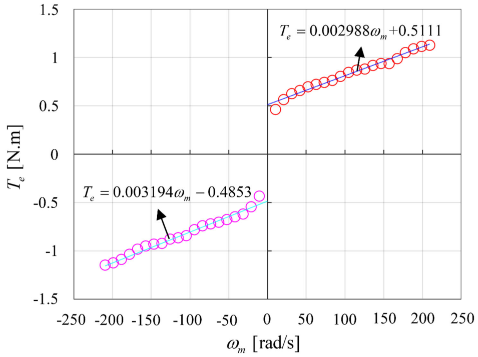

Fig. 20. Fitting of the friction coefficients on the test bench.

drivers; 2) a host computer with the software named Servo Tuning Platform, which is used for signal observation and debugging; 3) a parameter identification test-bed, including prototype PMSM, load PMSM, inertia pans, etc. The prototype PMSM is connected to the load PMSM, and these two PMSMs have the same parameters. The two drivers are used to drive the prototype PMSM and the load PMSM, respectively. Additionally, a position encoder of 2^{23} pulses/revolution is utilized to measure the real-time rotor position and speed. Under $i_d^* = 0$ control, T_e can be directly calculated using the equation $T_e = 1.5P_n\psi_f i_q$. The specification of the experimental platform is described in Table IV. According to Table IV, we can know that the total system inertia is $2\times$ $(1.061 \times 10^{-3} + 3 \times 1.108 \times 10^{-3} + 1.088 \times 10^{-3} + 0.08 \times 10^{-3}) + 6.321\times 10^{-5} = 11.17\times 10^{-3}$ Kg.m^2.

1) Fitting of Friction Coefficients: To evaluate the performance of our scheme, the viscous and Coulomb friction coefficients of the built experimental platform should be known. Under the no-load condition, these two friction coefficients can be calculated according to the fitting result of the relationship between T_e and ω_m [36]. To gain accurate results, T_e and ω_m corresponding to different speed commands are acquired in the cases of forward and reverse rotation for the prototype motor, respectively. Fig. 20 depicts the acquired T_e and ω_m. According to the obtained results, we can use the curve fitting method [36] to determine these two friction coefficients. As shown in Fig. 20, the fitting results are $T_e = 0.002988\omega_m + 0.5111$ and $T_e = 0.003194\omega_m - 0.4853$, respectively. Then, taking the average of the two fitting results, the viscous and Coulomb friction coefficients can be computed as $B = 0.003019$ N.m.s/rad and $C = 0.4982$ N.m, respectively.

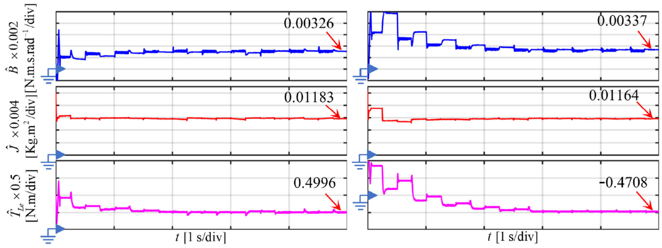

(a) (b)

Fig. 21. Experimental results under unidirectional speed commands. (a) Corresponding to the speed command $s^* = [\text{speed}(200, 2) + 200]$. (b) Corresponding to the speed command $s^* = [-\text{speed}(200, 2) - 200]$.

2) Main Parameter Settings: According to Section III, the network is designed with the following parameters: $k_1 = -2000$, $q_1 = 2.5$, $k_2 = -500$, $q_2 = 5\times10^{-6}$, $k_3 = -1000$, $q_3 = 1.2\times10^{-4}$. Additionally, in the experiments, the initial values of J, B, and T_L are randomly selected as $\hat{J}(0) = 0.02$ Kg.m^2, $\hat{T}_L(0) = 1$ N.m, and $\hat{B}(0) = 0.01$ N.m.s/rad, respectively. Note that in order to visually show the convergence rate and the influence of the initial values, the second step still selects these values as its initial values in our experiments.

3) Estimation of Coulomb Friction Coefficient: To estimate the Coulomb friction coefficient, one unidirectional speed command should be offered. Here, the speed command is chosen as $s^* = [\text{speed}(200, 2) + 200]$. In addition, the unidirectional speed command $s^* = [-\text{speed}(200, 2) - 200]$ is selected as a contrast speed. Fig. 21 depicts the estimation results under these two unidirectional speed commands. From Fig. 21, it can be seen that the estimated Coulomb friction coefficients under the two commands are determined as 0.4996 and 0.4708 N.m, respectively. It is noted that the estimated results are similar to the real Coulomb friction coefficient. Moreover, the identified system inertia and viscous friction coefficient are also close to their true values.

To reinforce the feasibility, repetitive experiments have been performed. Fig. 22 shows the estimation results under the two unidirectional speeds for 20 times repetitive experiments. In Fig. 22(a), the average of the estimated results is 0.5081 N.m, while the average is 0.4724 N.m in Fig. 22(b). By averaging these two values, the estimated Coulomb friction coefficient can be obtained as $\hat{C} = 0.4903$ N.m, which is very close to the fitting result. Note that this estimated value is used to calculate the real-time Coulomb friction torque in subsequent experiments.

4) Comparisons of Estimation Results With and Without Coulomb Friction Torque Compensation: Here, we choose the speed command as $s^* = [\text{speed}(800, 2) - 300]$. In addition, the load PMSM is used to generate 2-N.m load torque. Fig. 23 exhibits the comparison results. From there, we can see that $\hat{B} = 0.00514$ N.m.s/rad before the compensation (around 70% error), while $\hat{B} = 0.00326$ N.m.s/rad after the compensation

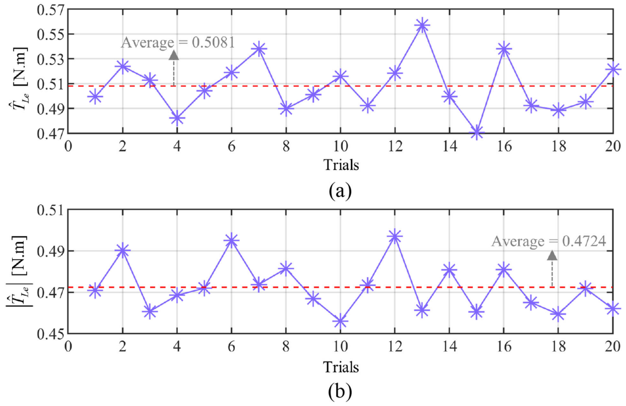

Fig. 22. Estimated Coulomb friction torque for 20 times repetitive experiments. (a) Corresponding to the command $s^* = [\text{speed}(200, 2) + 200]$. (b) Corresponding to the command $s^* = [-\text{speed}(200, 2) - 200]$.

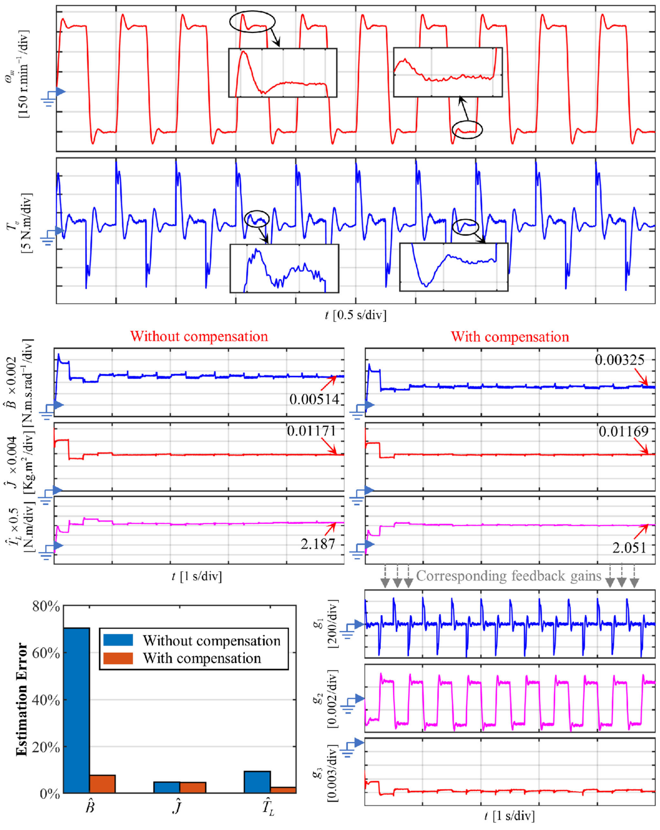

Fig. 23. Comparison of estimation results with and without Coulomb friction torque compensation.

(around 8% error). In Fig. 23, the estimation error of $\hat{T}_L$ before the compensation is 9.4%, while that after the compensation is 2.6%. It is noted that before and after compensation, the estimation error of $\hat{J}$ remains nearly constant (around 5% error). Overall, the abovementioned experimental phenomena agree well with those in the simulations, so the conclusion can be drawn. Additionally, Fig. 23 also shows the time-varying feedback gains, which guarantees the asymptotic convergence of the estimation errors.

TABLE V
CONFIGURATIONS OF Figs. 24 AND 25

Tests	Speed command (r/min)	Referenced load torque (N.m)
Figs. 24(a) and 24(d)	$s^* = [speed(400,2) + 200]$	Refe. $T_L = \begin{cases} 2 & (t \le 3\text{ s}) \\ 4 & (3 < t \le 7.5\text{ s}) \\ 1 & (7.5 < t \le 10\text{ s}) \end{cases}$
Figs. 24(b) and 24(e)	$s^* = [-speed(400,2) - 200]$	
Figs. 24(c) and 24(f)	$s^* = [speed(800,2) - 300]$	
Figs. 25(a) and 25(d)	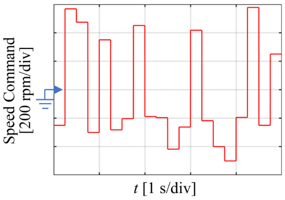 Speed Command [200 rpm/div] t [1 s/div]	Refe. $T_L = 2$
Figs. 25(b) and 25(e)		Refe. $T_L = \begin{cases} 2 & (t \le 2.5\text{ s}) \\ 1 & (2.5 < t \le 5\text{ s}) \end{cases}$
Figs. 25(c) and 25(f)		Refe. $T_L = \begin{cases} 2 & (t \le 2.5\text{ s}) \\ 3 & (2.5 < t \le 5\text{ s}) \end{cases}$

5) Comprehensive Performance Tests Under Regular and Random Speed Commands: To comprehensively evaluate the performance of the proposed scheme, we select regular and random speed commands to conduct experimental tests under the condition of time-varying load torque. Table V summarizes the given speed commands and the referenced load torques. Utilizing the previously estimated Coulomb friction coefficient ($\hat{C} = 0.4903$), the Coulomb friction torque can be calculated online, thus, being compensated. For comparison, the scheme proposed in [24] is also investigated under the same experimental conditions. Note that in related experiments, the parameters of this scheme are set as $k_1 = 55$, $k_2 = -1.5$, $k_J = 0.0004$, and $k_B = 0.15$. The corresponding estimation results are shown in Figs. 24 and 25. In Fig. 24, three different regular speed commands are selected. It can be found from Fig. 24 that, under regular speed commands, our scheme can estimate the three mechanical parameters more accurately than the technique presented in [24]. Actually, the method proposed in [24] suffers from quite significant estimation errors, as shown in Fig. 24(g). This results from the combined effects of neglecting Coulomb friction torque and poor robustness. In Fig. 25, the random speed commands are chosen. From there, it can be seen that our method can still gain more accurate estimation results compared with the method developed in [24]. It is worth noting that both Figs. 24 and 25 exhibit that our proposed scheme can accurately track the time-varying load torque. The abovementioned experimental phenomena verify the superior performance of the developed method.

In order to better compare the simulation and experimental results, we select the same initial values, referenced values, and speed commands as in Fig. 24(a)–(c) to conduct simulation studies. The corresponding simulation results are shown in Fig. 24(h)–(j). Compared with Fig. 24(a)–(c), it can be observed that the estimation errors of the experimental results are significantly higher than those of the simulation results. This is because the information on ω_m and T_e is not as accurate as in the simulation due to the system sampling errors and the inherent errors of the current and speed measurements. Moreover, the

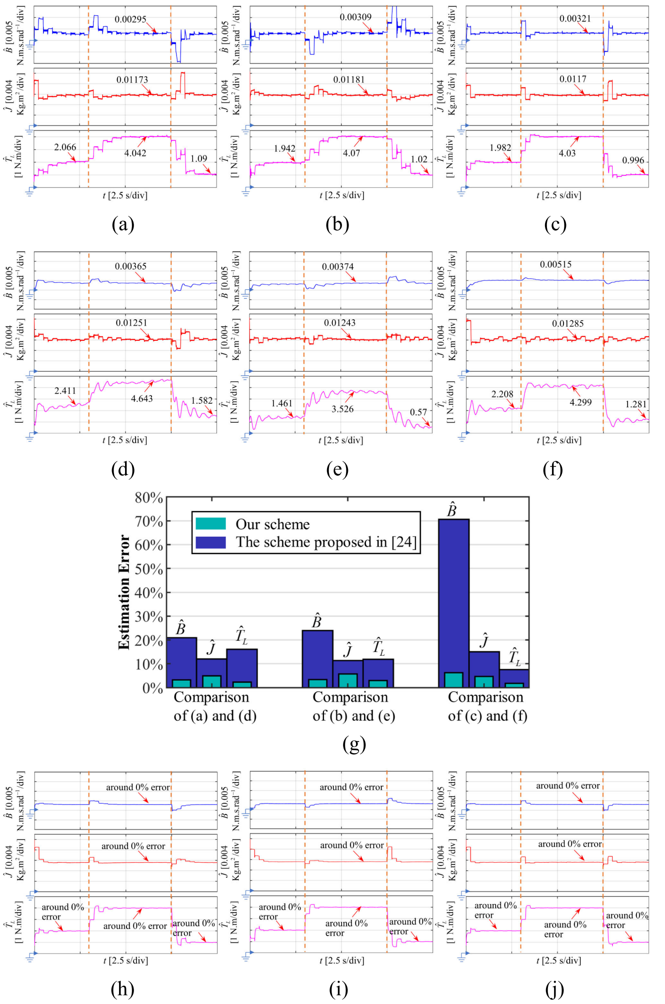

Fig. 24. Estimation results with regular speed commands under time-varying load torque. (a), (b), and (c) are the experimental results of our scheme. (d), (e), and (f) are the experimental results of the scheme proposed in [24]. (j) is the comparison of the estimation errors when $t \in [3, 7.5]$. (h), (i), and (j) are the simulation results corresponding to (a), (b), and (c), respectively.

system delay is also one of the sources of the estimation errors in the experiments. In addition, it should be noted that when the PMSM system encounters load disturbances, the convergence rates of $\hat{T}_L$ in the simulations are obviously faster than those in the experiments. One possible explanation is that in the experiments, the load torque needs to takes a certain amount of time to reach the given value due to the fact that it is generated by controlling the load motor.

In order to further test the effectiveness, two sets of random initial values are additionally selected to conduct experiments. For convenience, the previously used initial values are defined as $J_0 = 0.02$ Kg.m^2, $T_{L0} = 1$ N.m, and $B_0 = 0.01$ N.m.s/rad. Then, two sets of random initial values are chosen as follows. Test 1: The initial values of $\hat{J}, \hat{B}$, and $\hat{T}_L$ are chosen as $J_0^{'} = 5J_0$, $B_0^{'} = 5B_0$, and $T_{L0}^{'} = 5T_{L0}$; Test 2: The initial values of $\hat{J}, \hat{B}$, and $\hat{T}_L$ are chosen as $J_0^{''} = 0.2J_0$, $B_0^{''} = 0.2B_0$, and $T_{L0}^{''} = 0.2T_{L0}$. In addition, the speed command and the referenced load torque are consistent with those in

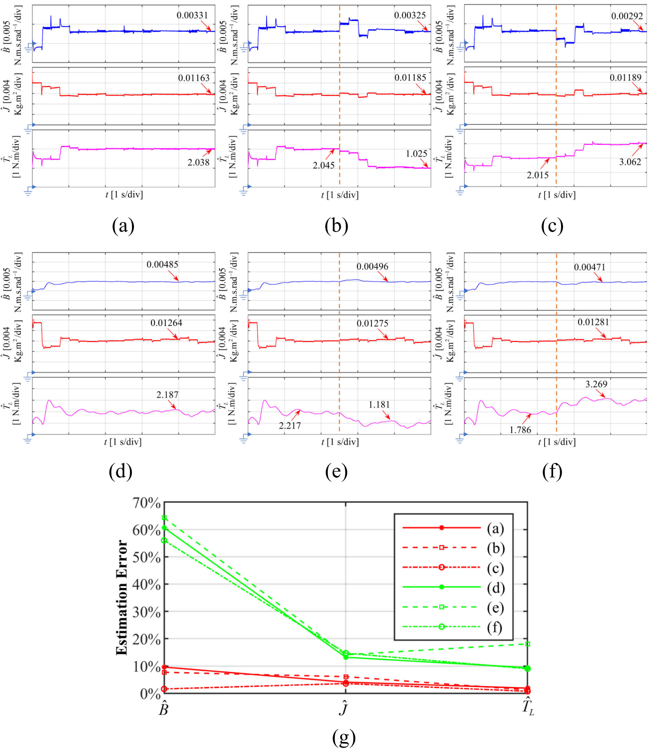

Fig. 25. Experimental results with random speed commands. (a), (b), and (c) are the estimated results of our scheme. (d), (e), and (f) are the identified results of the scheme proposed in [24]. (g) is the comparison of the estimation errors when $t \in [2.5, 5]$.

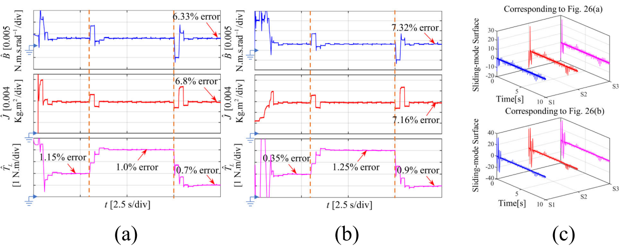

Fig. 26. Experimental results with different initial values. (a) At Test 1. (b) At Test 2. (c) Real-time changes of sliding-mode surfaces.

Fig. 24(c). The corresponding experimental results are shown in Fig. 26. The results manifest that our scheme can ensure the correct convergence of the estimation results under different initial conditions. In fact, due to the guarantee of Theorem 2, the estimation errors can tend to zero asymptotically with any initial conditions. In addition, Fig. 26(c) indicates that every sliding-mode surface is forced to stay in the area close to zero by the control of the network. This proves the occurrences of sliding modes, thus, laying the foundation for error convergence.

6) Effects of $q_i (i = 1, 2, 3)$ on Estimation Results: Here, related experiments are conducted to evaluate the detailed effects of the values of q_1, q_2, and q_3 on the estimation results. First, the speed command is chosen as $s^* = [\text{speed}(800, 2)\ -300]$. Second, let $q_{J0} = 2.5$, $q_{B0} = 5 \times 10^{-6}$, $q_{TL0} = 1.2 \times 10^{-4}$. In addition, the load PMSM is used to generate a constant load

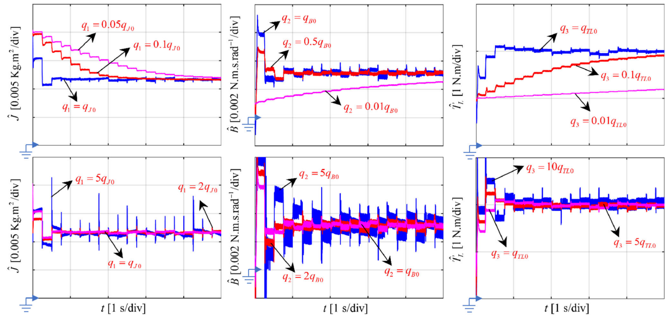

Fig. 27. Effects of different values of $q_i (i = 1, 2, 3)$ on the estimation results.

torque (2 N.m). Fig. 27 shows the effects of different values of q_1, q_2, and q_3 on the estimation results. From there, we can conclude that if $q_i (i = 1, 2, 3)$ is larger, the convergence rate is faster, and however, the estimation accuracy is lower. Meanwhile, a smaller $q_i (i = 1, 2, 3)$ means a smoother estimation result. These conclusions are in good agreement with the theoretical analysis in Section III. Therefore, in practical applications, we should select the appropriate values of $q_i (i = 1, 2, 3)$ to guarantee the fast convergence rate, weakened sliding-mode chattering, and high estimation accuracy.

7) Control Effects Test Case: The acquired $\hat{J}$ and $\hat{B}$ can be used to tune PI parameters [7], and the real-time $\hat{T}_L$ is beneficial for torque disturbance resistance [19]. These are classic performance optimization strategies in control practice. Here, we utilize the estimated parameters to implement these typical control designs to evaluate the performance of the PMSM system with the proposed parameter estimation method. Under $i_d^* = 0$ control, the speed-loop PI controller's proportional and integral gains can be designed as $k_p = J\omega_{sc}/k_t$ and $k_i = B\omega_{sc}/k_t$[7], where ω_{sc} is expected open-loop cutoff frequency of the speed loop, and $k_t = 1.5P_n\psi_f$. Thus, k_p and k_i can be tuned using the identified parameters ($\hat{J}$ and $\hat{B}$). When $\hat{T}_L$ is used for load torque feedforward control, the q-axis current command can be described as $i_q^* = i_{q\omega} + \hat{T}_L/k_t$, where $i_{q\omega}$ is the output of the speed-loop PI controller. Related experiments are done as follows.

In the first step of the proposed parameter estimation scheme, the speed command is selected as $s^* = [\text{speed}(200, 2) + 300]$, and then the estimation results shown in Fig. 28(a) can be obtained. Fig. 28(b) is the speed response after tuning the PI parameters using the acquired estimation results ($\hat{J} = 0.01178$ Kg.m^2 and $\hat{B} = 0.00315$ N.m.s/rad). From there, it can be seen that the speed control performance has been significantly enhanced after tuning. Fig. 29 shows the experimental results of load torque feedforward control utilizing the real-time $\hat{T}_L$ obtained from the second step of the parameter estimation scheme. Note that in the second step, the parameters acquired in the first step are set to the initial values, and the PI parameters adopt the values after tuning. Moreover, the speed command is set as $s^* = [\text{speed}(800, 2) \ -300]$, and the referenced load torque is increased from 2 to 4 N.m and then decreased from 4 to 3 N.m. It can be observed from Fig. 29 that after using $\hat{T}_L$ as the torque feedforward term, the speed error is smaller when encountering load disturbances. These results further demonstrate the validity of our proposed scheme. The abovementioned experiments are only a simple case concerning applying our scheme. Actually, our scheme can also be applied to many common control cases, including but not limited to online PI parameters self-tuning, advanced control strategy optimization (e.g., sliding-mode and predictive control), and PMSM system condition monitoring.

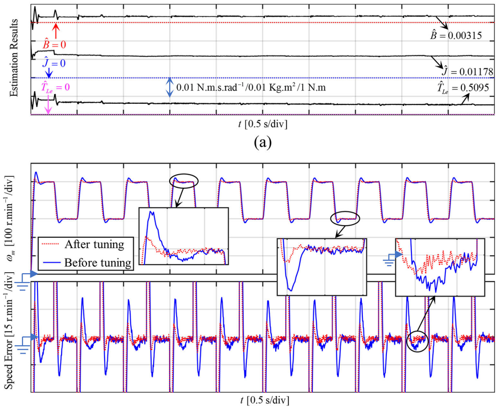

(a)

(b)

Fig. 28. Speed response before and after the PI parameters tuning. (a) Parameter estimation results. (b) Speed response comparison.

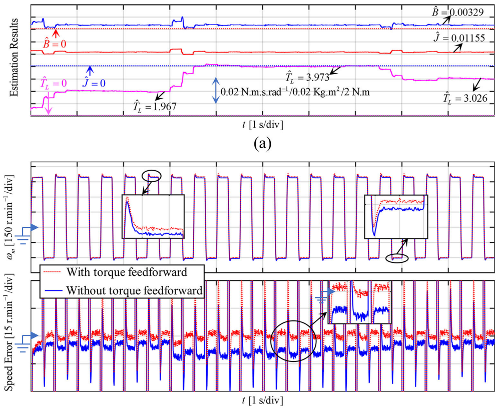

(a)

(b)

Fig. 29. Speed response with and without torque feedforward. (a) Parameter estimation results. (b) Speed response comparison.

V. CONCLUSION

In this article, an online parallel estimation scheme with a two-step mechanism is developed to accurately observe three mechanical parameters, including the viscous friction coefficient, the system inertia, and the load torque. This scheme is based on a network of three interconnected ESMOs. By utilizing the two-step mechanism, the adverse effect of the Coulomb friction torque on the estimation accuracy is removed effectively. The global stability of the parallel estimation is guaranteed, and the parameter estimation errors are forced to asymptotically toward zero without depending on any additional plant knowledge. Owing to the inherent LPF property, the sliding-mode chattering is weakened well, without requiring extra chattering attenuation.

Both simulation and real-time experimental results demonstrate that the presented scheme possesses fast-convergence and high-precision merits. In addition, the superiority of the proposed scheme is also seen in the fact that it is robust against noise. Future work should consider the auto-tuning of $q_i (i = 1, 2, 3)$ to seek better estimation performance and less parameter adjustment.

REFERENCES

[1] Q. Wang, G. Zhang, G. Wang, C. Li, and D. Xu, "Offline parameter self-learning method for general-purpose PMSM drives with estimation error compensation," *IEEE Trans. Power Electron.*, vol. 34, no. 11, pp. 11103–11115, Nov. 2019.

[2] Z. Liu, H. Wei, X. Li, K. Liu, and Q. Zhong, "Global identification of electrical and mechanical parameters in PMSM drive based on dynamic self-learning PSO," *IEEE Trans. Power Electron.*, vol. 33, no. 12, pp. 10858–10871, Dec. 2018.

[3] Z. Hao *et al.*, "Linear/nonlinear active disturbance rejection switching control for permanent magnet synchronous motors," *IEEE Trans. Power Electron.*, to be published.

[4] R. Garrido and A. Concha, "Inertia and friction estimation of a velocity-controlled servo using position measurements," *IEEE Trans. Ind. Electron.*, vol. 61, no. 9, pp. 4759–4770, Sep. 2014.

[5] F.-J. Lin, S.-G. Chen, S. Li, H.-T. Chou, and J.-R. Lin, "Online autotuning technique for IPMSM servo drive by intelligent identification of moment of inertia," *IEEE Trans. Ind. Informat.*, vol. 16, no. 12, pp. 7579–7590, Dec. 2020.

[6] Y. Feng, X. Yu, and F. Han, "High-order terminal sliding-mode observer for parameter estimation of a permanent-magnet synchronous motor," *IEEE Trans. Ind. Electron.*, vol. 60, no. 10, pp. 4272–4280, May 2013.

[7] X. Zhang and Z. Li, "Sliding-mode observer-based mechanical parameter estimation for permanent magnet synchronous motor," *IEEE Trans. Power Electron.*, vol. 31, no. 8, pp. 5732–5745, Mar. 2016.

[8] M. Shao, Y. Deng, H. Li, J. Liu, and Q. Fei, "Sliding mode observer-based parameter identification and disturbance compensation for optimizing the model predictive control of PMSM," *Energies*, vol. 12, no. 10, May 2019, Art. no. 1857.

[9] H. Kim, H. Kim, and J. Choi, "Multiparameter identification for SPMSMs using NLMS adaptive filters and extended sliding-mode observer," *IET Electr. Power Appl.*, vol. 14, no. 4, pp. 533–543, Apr. 2020.

[10] L. Salvatore and S. Stasi, "Application of EKF to parameter and state estimation of PMSM drive," *IEE Proc. B Electr. Power Appl.*, vol. 139, no. 3, pp. 155–164, May 1992.

[11] T. Boileau, N. Leboeuf, B. Nahid-Mobarakeh, and F. Meibody-Tabar, "Online identification of PMSM parameters: Parameter identifiability and estimator comparative study," *IEEE Trans. Ind. Appl.*, vol. 47, no. 4, pp. 1944–1957, Jul./Aug. 2011.

[12] K. Liu and Z. Zhu, "Fast determination of moment of inertia of permanent magnet synchronous machine drives for design of speed loop regulator," *IEEE Trans. Control Syst. Technol.*, vol. 25, no. 5, pp. 1816–1824, Sep. 2017.

[13] O. C. Kivanc and S. B. Ozturk, "Sensorless PMSM drive based on stator feedforward voltage estimation improved with MRAS multiparameter estimation," *IEEE/ASME Trans. Mechatron.*, vol. 23, no. 3, pp. 1326–1337, Jun. 2018.

[14] F.-J. Lin, "Robust speed-controlled induction-motor drive using EKF and RLS estimators," *IEE Proc.–Electr. Power Appl.*, vol. 143, no. 3, pp. 186–192, 1996.

[15] S. J. Underwood and I. Husain, "Online parameter estimation and adaptive control of permanent-magnet synchronous machines," *IEEE Trans. Ind. Electron.*, vol. 57, no. 7, pp. 2435–2443, Jul. 2010.

[16] N. Lozada-Castillo, I. Chairez, A. Luviano-Juárez, and J. Escobar, "Parameter identification of a permanent magnet synchronous motor," in *Proc. 53rd IEEE Conference Decision Control*, Los Angeles, CA, USA, 2014, pp. 1005–1010.

[17] J. Linares-Flores, A. Hernández Méndez, C. García-Rodríguez, and H. Sira-Ramírez, "Robust nonlinear adaptive control of a 'boost' converter via algebraic parameter identification," *IEEE Tran. Ind. Electron.*, vol. 61, no. 8, pp. 4105–4114, Aug. 2014.

[18] L. Niu, D. Xu, M. Yang, X. Gui, and Z. Liu, "On-line inertia identification algorithm for PI parameters optimization in speed loop," *IEEE Trans. Power Electron.*, vol. 30, no. 2, pp. 849–859, Feb. 2015.

[19] C. Lian, F. Xiao, S. Gao, and J. Liu, "Load torque and moment of inertia identification for permanent magnet synchronous motor drives based on sliding mode observer," *IEEE Trans. Power Electron.*, vol. 34, no. 6, pp. 5675–5683, Jun. 2019.

[20] M. Yang, Z. Liu, J. Long, W. Qu, and D. Xu, "An algorithm for online inertia identification and load torque observation via adaptive kalman observer-recursive least squares," *Energies*, vol. 11, no. 4, pp. 1–17, Mar. 2018.

[21] X. Wang, S. Xu, G. Jing, Q. An, S. Li, and L. Sun, "Low-speed performance improvement of permanent magnet synchronous motor drive based on nonlinear disturbance torque observer," in *Proc. 22nd Int. Conf. Electr. Mach. Syst.*, Harbin, China, 2019, pp. 1–5.

[22] J. Jin, S. Wang, and S. Huang, "Adaptive disturbance observer design for servo drive system with time-varying load inertia," in *Proc. IEEE Int. Conf. Mechatronics Autom.*, Tianjin, China, 2014, pp. 1504–1508.

[23] W. Huang, C. Liu, P. Hsu, and S. Yeh, "Precision control and compensation of servomotors and machine tools via the disturbance observer," *IEEE Trans. Ind. Electron.*, vol. 57, no. 1, pp. 420–429, Oct. 2010.

[24] S. Zhao, Y. Chen, and Y. Mao, "Adaptive load observer-based feed-forward control in PMSM drive system," *Trans. Inst. Meas. Control.*, vol. 37, no. 3, pp. 414–424, Aug. 2014.

[25] B. Yao, Z. Zhou, L. Wang, W. Xu, Q. Liu, and A. Liu, "Sensorless and adaptive admittance control of industrial robot in physical human-robot interaction," *Robot. Comput. Integr. Manuf.*, vol. 51, pp. 158–168, Jun. 2018.

[26] Y. Yu, Z. Mi, X. Guo, Y. Xu, and T. Zhao, "Low speed control and implementation of permanent magnet synchronous motor for mechanical elastic energy storage device with simultaneous variations of inertia and torque," *IET Electr. Power Appl.*, vol. 10, no. 3, pp. 172–180, Mar. 2016.

[27] N. Borchardt, R. Hinzelmann, D. S. Pucula, W. Heinemann, and R. Kasper, "Winding machine for automated production of an innovative air-gap winding for lightweight electric machines," *IEEE/ASME Trans. Mechatron.*, vol. 21, no. 3, pp. 1509–1517, Jun. 2016.

[28] L. Márton, "On-line lubricant health monitoring in robot actuators," in *Proc. Australian Control Conf.*, Melbourne, VIC, Australia, 2011, pp. 167–172.

[29] L. Márton and F. van der Linden, "Temperature dependent friction estimation: Application to lubricant health monitoring," *Mechatronics*, vol. 22, no. 8, pp. 1078–1084, Dec. 2012.

[30] H. H. Choi and J. Jung, "Fuzzy speed control with an acceleration observer for a permanent magnet synchronous motor," *Nonlinear Dyn.*, vol. 67, no. 3, pp. 1717–1727, Jun. 2011.

[31] H. H. Choi and J. Jung, "Discrete-time fuzzy speed regulator design for PM synchronous motor," *IEEE Trans. Ind. Electron.*, vol. 60, no. 2, pp. 600–607, Feb. 2013.

[32] S. Kim, "Moment of inertia and friction torque coefficient identification in a servo drive system," *IEEE Trans. Ind. Electron.*, vol. 66, no. 1, pp. 60–70, Jan. 2019.

[33] Y. Zuo, J. Mei, X. Zhang, and C. H. T. Lee, "Simultaneous identification of multiple mechanical parameters in a servo drive system using only one speed," *IEEE Trans. Power Electron.*, vol. 36, no. 1, pp. 716–726, Jan. 2021.

[34] W. Zhang, B. Cao, N. Nan, M. Li, and Y. Chen, "An adaptive PID-type sliding mode learning compensation of torque ripple in PMSM position servo systems towards energy efficiency," *ISA Trans.,* vol. 110, pp. 258–270, Oct. 2020.

[35] J. Liu, H. Li, and Y. Deng, "Torque ripple minimization of PMSM based on robust ILC via adaptive sliding mode control," *IEEE Trans. Power Electron.*, vol. 33, no. 4, pp. 3655–3671, Apr. 2018.

[36] K. Liu, C. Hou, and W. Hua, "A novel inertia identification method and its application in PI controllers of PMSM drives," *IEEE Access*, vol. 7, pp. 13445–13454, Jan. 2019.

Chengbo Yang (Student Member, IEEE) received the B.S. degree in mechanical design manufacturing and automation from Southwest University, Chongqing, China, in 2018. He is currently working toward the Ph.D. degree in mechanical engineering with the Huazhong University of Science and Technology, Wuhan, China.

His research interests include parameter estimation, servo control, and intelligent technology.

Bao Song received the Ph.D. degree in mechanical engineering from the Huazhong University of Science and Technology (HUST), Wuhan, China, in 2005.

From 2006 to 2008, she performed postdoctoral research with The Hong Kong University of Science and Technology, Hong Kong. She is currently a Professor with the School of Mechanical Science and Engineering, HUST. She has authored and coauthored more than 50 academic papers and obtained more than 20 invention patents. Her research interests include servo control, parameter estimation, and field-bus technology.

Yuanlong Xie (Member, IEEE) received the B.S. degree in electrical engineering and the Ph.D. degree in mechanical engineering from the Huazhong University of Science and Technology (HUST), Wuhan, China, in 2014 and 2018, respectively.

From 2017 to 2018, he was an Academic Visitor with the School of Electronic and Electrical Engineering, University of Leeds, Leeds, U.K. Since November 2018, he has been a Postdoctoral Fellow with HUST. He has authored and coauthored more than 60 academic journal and conference papers, one book, and held more than 15 patents. His research interests include robot control, servo control, filed-bus technology, and networked control systems.

Dr. Xie received the Best Student Paper Award at the 2020 IEEE Region 10 Conference.

Xiaoqi Tang received the Ph.D. degree in mechanical engineering from the Huazhong University of Science and Technology (HUST), Wuhan, China, in 1998.

From 1996 to 1998, he was an Academic Visitor with the School of Engineering, The Hong Kong University of Science and Technology, Hong Kong, China. He is currently a Professor with HUST and a Vice Director of the National NC System Engineering Research Center. He has authored or coauthored more than 100 academic papers and gained more than 40 invention patents. His research interests include servo drives, NC technology, industrial robot control, and intelligent machinery manufacturing.